Monthly Notices
of the
ROYAL ASTRONOMICAL SOCIETY

MNRAS **450,** 4248–4276 (2015) doi:10.1093/mnras/stv783

Optical and Sunyaev–Zel'dovich observations of a new sample of distant rich galaxy clusters in the *ROSAT* All Sky

A. Buddendiek,[1⋆] T. Schrabback,[1,2,3] C. H. Greer,[4] H. Hoekstra,[2] M. Sommer,[1] T. Eifler,[5,6] T. Erben,[1] J. Erler,[1] A. K. Hicks,[7] F. W. High,[8] H. Hildebrandt,[1] D. P. Marrone,[4] R. G. Morris,[3,9] A. Muzzin,[2] T. H. Reiprich,[1] M. Schirmer,[10] P. Schneider[1] and A. von der Linden[3,11,12]

[1] *Argelander-Institut für Astronomie, Rheinische Friedrich-Wilhelms-Universität Bonn, Auf dem Hügel 71, D-53121 Bonn, Germany*
[2] *Leiden Observatory, Leiden University, PO Box 9513, NL-2300 RA Leiden, the Netherlands*
[3] *Kavli Institute for Particle Astrophysics and Cosmology, Stanford University, 452 Lomita Mall, Stanford, CA 94305-4085, USA*
[4] *Steward Observatory, University of Arizona, Tuscon, AZ 85121, USA*
[5] *Jet Propulsion Laboratory, California Institute of Technology, 4800 Oak Grove Dr, Pasadena, CA 91109, USA*
[6] *Center for Cosmology and Astro-Particle Physics, The Ohio State University, 191 W. Woodruff Ave, Columbus, 43210 OH, USA*
[7] *Eureka Scientific, 2452 Delmer Street, Suite 100, Oakland, CA 94602-3017, USA*
[8] *Kavli Institute for Cosmological Physics, University of Chicago, 5640 South Ellis Avenue, Chicago, IL 60637, USA*
[9] *SLAC National Accelerator Laboratory, 2575 Sand Hill Road, Menlo Park, CA 94025, USA*
[10] *Gemini Observatory, Casilla 603, La Serena, Chile*
[11] *Dark Cosmology Centre, Niels Bohr Institute, University of Copenhagen Juliane Maries Vej 30, DK-2100 Copenhagen Ø, Denmark*
[12] *Department of Physics, Stanford University, 382 Via Pueblo Mall, Stanford, CA 94305-4060, USA*

Accepted 2015 April 2. Received 2015 March 20; in original form 2014 December 10

ABSTRACT

Finding a sample of the most massive clusters with redshifts $z > 0.6$ can provide an interesting consistency check of the Λ cold dark matter (ΛCDM) model. Here, we present results from our search for clusters with $0.6 \lesssim z \lesssim 1.0$ where the initial candidates were selected by cross-correlating the ROSAT All Sky Survey (RASS) faint and bright source catalogues with red galaxies from the Sloan Digital Sky Survey DR8. Our survey thus covers $\approx$10 000 deg^2, much larger than previous studies of this kind. Deeper follow-up observations in three bands using the William Herschel Telescope and the Large Binocular Telescope were performed to confirm the candidates, resulting in a sample of 44 clusters for which we present richnesses and red sequence redshifts, as well as spectroscopic redshifts for a subset. At least two of the clusters in our sample are comparable in richness to RCS2-*J*232727.7−020437, one of the richest systems discovered to date. We also obtained new observations with the Combined Array for Research in Millimeter Astronomy for a subsample of 21 clusters. For 11 of those we detect the Sunyaev–Zel'dovich effect signature. The Sunyaev–Zel'dovich signal allows us to estimate M_{200} and check for tension with the cosmological standard model. We find no tension between our cluster masses and the ΛCDM model.

Key words: cosmology: observations.

1 INTRODUCTION

Clusters of galaxies, especially at high redshift, are important tools to study our Universe. Years before the discovery of dark energy in the late 20th century cluster studies already pointed towards an Ω_{m} much smaller than unity (e.g. White et al. 1993; Bahcall, Lubin & Dorman 1995). Furthermore, one can measure the total number of clusters per mass bin and compare it to theoretical predictions.

In order to conduct such a cosmological analysis of a sample of galaxy clusters one first has to find them. Galaxy cluster detection is possible in many different ways depending on the wavelength. Since the intra-cluster medium (ICM) emits in the X-ray one can use X-ray surveys to detect clusters. This has been done many times using different X-ray observatories. For example using the *ROSAT* satellite (e.g. XBAC: Ebeling et al. 1996; BCS: Ebeling et al. 1998; MACS: Ebeling, Edge & Henry 2001b; HIFLUGCS: Reiprich & Böhringer 2002; 400D Cluster Survey: Burenin et al. 2007) or the *XMM–Newton* satellite (e.g. XCS: Romer et al. 2001; Mehrtens et al. 2012; XMM LSS: Pierre et al. 2001; Pierre, Valtchanov & Refregier

---

[⋆] E-mail: abuddend@astro.uni-bonn.de

Published by Oxford University Press on behalf of the Royal Astronomical Society

2002; REXCESS: Böhringer et al. 2007). Using the X-ray emission of the ICM one can measure the temperature of the gas, which probes the full gravitational potential of the cluster. Consequently, the X-ray properties of clusters correlate well with mass (e.g. Mahdavi et al. 2013). Once redshift, mass, and the selection function are known the samples can be used for constraining cosmological parameters (e.g. Vikhlinin et al. 2009; Mantz et al. 2014).

Also, cosmic microwave background (CMB) photons experience inverse Compton scattering due to the electrons in the ICM and thus the CMB spectrum changes. Depending on the frequency one will either observe a decrease in photons or an increase. This is known as the Sunyaev–Zel'dovich effect (SZE; Sunyaev & Zeldovich 1970, 1980). The SZE is also being used as another way to find galaxy clusters for example by the South Pole Telescope (SPT; e.g. Bleem et al. 2015), the Atacama Cosmology Telescope (ACT; e.g. Hasselfield et al. 2013) or the *Planck* satellite (Planck Collaboration XXVII 2015). The SZE probes the integrated pressure of the ICM, which probes the gravitational potential and has also been found to correlate well with mass (e.g. Bonamente et al. 2008). SZ-selected samples have been used for cosmological parameter constraints (e.g. Benson et al. 2013; Sievers et al. 2013; Planck Collaboration XXIV 2015).

Galaxy cluster detection in the optical works somewhat differently. Most cluster finding algorithms look for overdensities in the galaxy distribution. Nowadays, this is usually combined with magnitude information or photometric redshifts (e.g. Postman et al. 1996; Milkeraitis et al. 2010). Similar to photometric redshifts one can also use colour information and an intrinsic property of clusters, the cluster red sequence. This red sequence can be observed as a region in the colour–magnitude diagram, where red galaxies of the same cluster align along a line of almost constant colour (Gladders & Yee 2000). This is due to the redshift dependent shift of the 4000 Å-break through the filter bands in use, which is why the location of the red sequence in colour–magnitude space can be used as an estimator for the cluster redshift.

The red sequence method has also been used for cluster detection for example by the Red Cluster Sequence Surveys 1 and 2 (Gladders & Yee 2005; Gilbank et al. 2011), by the MaxBCG programme (Koester et al. 2007), or redMaPPer (Rykoff et al. 2014). Besides giving an estimate for the cluster redshift optical surveys can also provide estimates of 'cluster richness', which is the number of cluster galaxies within a certain radius and brighter than some characteristic magnitude. Several cluster surveys have been generated around various richness measures (e.g. Koester et al. 2007; High et al. 2010; Rykoff et al. 2014) and it has been shown to correlate with mass (e.g. Planck Collaboration XII 2011, Sehgal et al. 2013) although this relation appears to have large intrinsic scatter (Angulo et al. 2012).

Usually, the methods of cluster detection that do not make use of optical observations require some kind of confirmation from a different wavelength regime. This can be overcome by cross-correlating data from two different regimes. This has been done using optical and X-ray data by for example the Massive Cluster Survey (MACS; Ebeling et al. 2001b), the ROSAT All Sky Survey (RASS)-SDSS Galaxy Cluster Survey (Popesso et al. 2004), or the extended MACS (eMACS; Ebeling et al. 2013). Also optical and infrared data have been combined by the Massive Distant Clusters of Wise Survey (Brodwin et al. 2014).

The most extreme clusters in mass ($M_{200} \geq 5 \times 10^{14}\,\mathrm{M}_{\odot}$) can be used for a cosmological test other than cluster counting. Given a cosmological model one can compute the allowed masses of galaxy clusters as a function of redshift (Haiman, Mohr & Holder 2001; Weller, Battye & Kneissl 2002). This probes the extreme end of the mass function. In order to systematically search for the most massive clusters in our Universe a deep and wide area survey that probes large volumes needs to be carried out. Until recently, mostly samples consisting of only a few clusters that were discovered in small surveys were tested for consistency with the Λ cold dark matter (ΛCDM) model. For example, Broadhurst & Barkana (2008) used mass estimates based on strong lensing arcs of four galaxy clusters, whereas Jee et al. (2011) used weak gravitational lensing masses of 22 clusters. In Mortonson, Hu & Huterer (2011) two clusters are tested and the authors provide a fitting formula for exclusion curves, which was shown to be too strict by Hotchkiss (2011). In contrast to testing single cluster masses for consistency with the standard cosmological model one can also use extreme number statistics and test a whole sample of clusters (Waizmann, Redlich & Bartelmann 2012; Waizmann, Ettori & Bartelmann 2013). So far only Jee et al. (2011) find significant deviations from ΛCDM, using the exclusion curves from Mortonson et al. (2011). Considering the findings of Hotchkiss (2011) this tension has likely been resolved.

In the last years more large volume surveys were conducted. Especially the *Planck* satellite has been shown to find massive galaxy clusters at redshifts greater than $z = 0.5$ (Planck Collaboration XXIX 2014) spread over the whole sky. This is complementary to the samples found by the SPT (Bleem et al. 2015) and ACT (Hasselfield et al. 2013), which originate from a smaller area and consist of typically slightly less massive but higher redshift clusters.

This work is meant to be a continuation of the still ongoing search for massive galaxy clusters at high redshift. By cross-correlating the positions of red galaxies in the Sloan Digital Sky Survey (SDSS) and the faint and bright source catalogues of RASS, we create a new sample of distant ($z > 0.6$) and possibly massive cluster candidates, making use of the wide area of the SDSS Data Release 8. Because red galaxies are known to reside preferentially in clusters, this is a useful approach to identify massive clusters from the RASS catalogues which are strongly contaminated with other X-ray sources (for example AGN or binary stars). Through follow-up observations using the William Herschel Telescope (WHT), the Large Binocular Telescope (LBT), and the Combined Array for Research in Millimeter Astronomy (CARMA), we then confirm or reject our candidates and check for consistency with ΛCDM. This study presents one of the first systematic searches for massive high-redshift galaxy clusters in the optical and X-ray regimes in a very large volume. Similar approaches to detect clusters have been used for eMACS (Ebeling et al. 2013), which also uses RASS data but for the optical part it makes use of deeper imaging data from the Pan-STARRS Medium Deep Survey, which is part of the Pan-STARRS project (Kaiser et al. 2002). Also, the aforementioned work by Brodwin et al. (2014) searches for high-redshift clusters in data from the *Wide-Field Infrared Survey Explorer* satellite (Wright et al. 2010). Instead of cross-correlating with optical data they use a non-detection in the SDSS as an indication for a high-redshift cluster.

One should note that we do not intend to use our sample for cosmological cluster abundance studies. By specifically following up the most extreme candidates we compromise a simple selection function. None the less, it is one of the largest samples of very X-ray-luminous high-redshift galaxy clusters in the Northern hemisphere making it complementary to the cluster samples found by *Planck*, SPT, and ACT. The distribution of all clusters in our sample on the sky is plotted in Fig. 1.

In Section 2, we first describe how we define our cluster sample. We then explain the data from follow-up observations and the

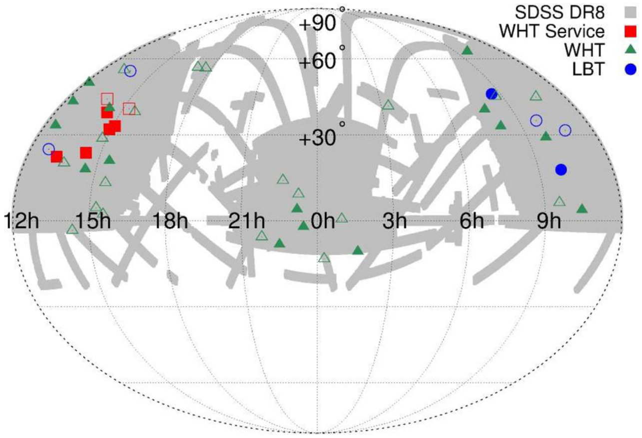

Figure 1. This plot shows the distribution of all clusters of our sample on the sky. Open symbols indicate clusters with unknown spectroscopic redshift. Our search for clusters makes use of about one quarter of the whole sky.

instruments which were used for those campaigns in Section 3. This is followed by a detailed description about the red sequence and richness analysis and their interpretation in Section 4. We describe the SZ data analysis in Section 5. In Section 6, we discuss possible tensions of our cluster sample with ΛCDM, and in Section 7 properties of some individual clusters. This is followed by our conclusion. Images showing postage stamps of all 47 clusters, including three previously discovered objects, as well as SZ-maps from CARMA and *Planck* data can be found in the appendix.

As our fiducial cosmology, we use $H_0 = 70\,\mathrm{km\,Mpc^{-1}\,s^{-1}}$, $h = 0.7$, $\Omega_\Lambda = 0.7$ and $\Omega_\mathrm{m} = 0.3$. The exclusion plots in Section 6 were created assuming $\sigma_8 = 0.83$ as has been done in Mortonson et al. (2011). We define r_{500} (r_{200}) as the radius, where the density of the galaxy cluster is 500 (200) times the critical density of the universe.

2 PRE-SELECTION OF CLUSTER CANDIDATES

To find some of the most massive clusters at redshifts $0.6 \lesssim z \lesssim 1.0$, we use the combined bright and faint source catalogues of RASS (Voges et al. 1999;[1] Voges et al. 2000[2]), which is an X-ray all sky survey in the 0.1–2.4 keV range carried out with the *ROSAT* satellite. This combined catalogue contains 125 000 entries with typical positional uncertainties of 20 arcsec. Most of these objects are not galaxy clusters but rather AGN or X-ray binaries. Hence, to identify distant galaxy clusters, more information is needed. For that we combine the X-ray data with imaging data from the SDSS (Castander 1998), where we used Data Release 8 (Aihara et al. 2011). By cross-correlating the RASS object positions with the position of SDSS galaxies for which the SDSS photometry suggests that they likely match the targeted redshift range, we are able to efficiently preselect candidates for galaxy clusters. Here, we generally use a 50 arcsec matching radius, which should account for the positional uncertainty in RASS and for the fact that galaxies scatter around the cluster centre. Note that we did not employ a radius in projected physical separation given the photometric redshift uncertainties and the small change in projected radius of only about 50 kpc between $z = 0.6$ and 0.9. Photometric redshifts are taken from the `Photoz`-table in the SDSS archive. We then employ two different SDSS galaxy selection schemes: In the first scheme, we select all SDSS galaxies with a photometric redshift $z > 0.6$ and $i < 20.5$. This yields 1149 matches of RASS sources with two or more SDSS DR8 galaxies, mostly at $0.6 \lesssim z \lesssim 0.8$. At higher redshifts, we expect that possibly only a single cluster galaxy [the brightest cluster galaxy (BCG)] is detected in SDSS. We select candidates for such galaxies photometrically from SDSS with colour cuts $r - i > 0.5$, $i - z > 0.8$, and $17 < i < 21$ (compare e.g. High et al. 2010). While requiring a match of at least one of these galaxies in the SDSS DR8 with the RASS sources and adding these cases to our preselected sample we find 1395 candidates in total.

In the next step all candidates are visually inspected using SDSS postage stamps and graded. Here, we immediately drop obvious chance alignments of background galaxies e.g. with bright foreground stars, spectroscopically classified quasi stellar objects (QSOs), or low-z galaxy groups, which most likely dominate the X-ray flux. In addition, we drop sparse galaxy groups/clusters, where the SDSS colours suggest $z \sim 0.6$–0.7. At these redshifts, we would still expect to detect numerous cluster galaxies in SDSS if these were massive clusters. Hence, these sparse groups/clusters likely have an X-ray flux boosted by an AGN and are not of interest for our study. The remaining candidates are graded in preparation for further follow-up observations (Section 3), where we prioritize the richest systems as well as good candidates for the highest redshift clusters ($z \gtrsim 0.8$) in our sample. We attempted optical follow-up observations for a total of 80 candidates. From these 48 have data of sufficient quality in the three filters r, i, z, constituting the sample we analyse in this paper. This includes all of the top-graded candidates. For eight of the remaining candidates, single-band observations were sufficient to identify them as false positive. The remaining 24 candidates, which were all of lower or medium priority, were dropped from the current analysis, as they do not have observations of sufficient quality in all three bands. This was due to observations attempted under poor conditions, guiding errors, or limited target visibility. Within the allocated time these observations could not be completed or repeated, but we ensured to complete the observations for all of the highly graded candidates.

With our automated pre-selection, we also ‘rediscovered’ the known massive clusters MACS*J*0744.8+3927 ($z = 0.6976$; Ebeling et al. 2007), MACS*J*2129.4−0741 ($z = 0.5889$; Ebeling et al. 2007), and RCS2-*J*232727.7−020437, ($z = 0.705$; Menanteau et al. 2013), providing a confirmation of our algorithm and a reference sample of massive clusters in the targeted redshift range.

3 FOLLOW-UP OBSERVATIONS

3.1 Optical images

3.1.1 William Herschel Telescope

The majority of our optical follow-up observations were taken with the Auxiliary-port CAMera (ACAM; Benn, Dee & Agócs 2008) on the 4.2-m WHT on the island of La Palma in Spain. ACAM is a red-optimized one chip camera with 2148 × 2500 pixels which has an unvignetted circular field of view of about 8 arcmin in diameter and a pixel scale of 0.25 arcsec.

Our WHT data were taken in service mode (2010 August and 2013 August, PIs Schrabback and Buddendiek, respectively), and in visitor mode (four nights each in 2011 August and 2012 March, PI Schrabback). We obtained imaging in r, i, and z filters, which

---

[1] http://www.xray.mpe.mpg.de/rosat/survey/rass-bsc/

[2] http://www.xray.mpe.mpg.de/rosat/survey/rass-fsc/

Table 1. The spectroscopic sub-sample. Spectroscopic redshifts are either measured from our data, taken from independent discoveries or from the SDSS DR 10. If z_{spec} was measured, the spectroscopic features which were identified by visually inspecting the spectra are listed. For ClG-*J*131339.7+221151, we downloaded one spectrum from the SDSS data base and determined the redshift ourselves, because the estimate taken from SDSS proved not to be trustworthy ($z_{\mathrm{SDSS}} = 1.000 \pm 3.359$).

Object	Redshift	Lines	# Spectra	Ref.
ClG-*J*013710.4−103423	0.662 ± 0.002	Ca H+K, 4000 Å	1	–
ClG-*J*031924.2+404055	0.680 ± 0.003	Ca H+K, 4000 Å	1	–
MACSJ0744.8+3927^a	0.698	–	–	Ebeling et al. (2007)
ClG-*J*080434.9+330509	0.553	–	1	SDSS
ClG-*J*083415.3+452418	0.666	–	1	SDSS
ClG-*J*094700.0+631905	0.710	–	1	SDSS
ClG-*J*094811.6+290709	0.778 ± 0.002	Ca H+K, 4000 Å	1	–
ClG-*J*095416.5+173808	0.828	–	–	Nastasi et al. (2014)
ClG-*J*102714.5+034500	0.749 ± 0.003	Ca H+K, 4000 Å	1	–
ClG-*J*120958.9+495352	0.902 ± 0.001	[O II], Ca H+K	1	–
ClG-*J*122208.6+422924	1.069 ± 0.003	Ca H+K, 4000 Å	2	–
Cl*J*1226.9+3332^a	0.892	–	–	Ebeling et al. (2001a)
ClG-*J*131339.7+221151	0.737 ± 0.002	Ca H+K, 4000 Å	1	SDSS
ClG-*J*142040.3+395509	0.607	–	–	Bayliss et al. (2011)
ClG-*J*142138.3+382118	0.762	–	1	SDSS
ClG-*J*142227.4+233739	0.726	–	1	SDSS
ClG-*J*143411.9+175039	0.744 ± 0.003	Ca H+K, 4000 Å	1	–
ClG-*J*145508.4+320028	0.654	–	1	SDSS
ClG-*J*150532.2+331249	0.758	–	1	SDSS
ClG-*J*152741.9+204443	0.693 ± 0.002	Ca H+K, 4000 Å	1	–
ClG-*J*223007.6−080949	0.623 ± 0.003	Ca H+K, 4000 Å	1	–
ClG-*J*231215.6+035307	0.648 ± 0.003	[O II], Ca H+K, 4000 Å	4	–
RCS2-*J*232727.7−020437^a	0.705	–	–	Menanteau et al. (2013)

Note. ^{a}These clusters were known before and are only included in the sample for calibration reasons.

bracket the 4000 Å-break in the redshift range of interest. The service observations in 2010 were carried out with the RGOZ2 filter ($\lambda_{\mathrm{central}} = 8748$ Å) as the SDSS z-band was not yet available. Therefore, we need to create different red sequence models for those images later on. Our total exposure time per cluster candidate per filter varies between 360 and 1800 s, this choice primarily depends on observing conditions and the roughly estimated cluster redshift. For some of the candidates for the highest redshift clusters in the sample – which typically were the most uncertain candidates with only a single noisy BCG candidate – we stopped observing after taking data in a single filter (i or z) if these data clearly showed that this was a spurious match (e.g. a faint red star misclassified as galaxy in SDSS). In total, we obtained three-band imaging for 42 cluster candidates with ACAM, plus three previously known clusters with spectroscopic redshifts which were included as reference objects for the generation of the red sequence model (see Table 1).

3.1.2 *Large Binocular Telescope*

We observed nine cluster candidates using the 2 × 8.4-m LBT in Arizona during observations in 2010 October and December, as well as 2011 February and April (PI: Eifler). Two of these candidates were also observed with the WHT. Here we employed the r-, i- and z-filters, which are similar to the WHT filters used. The instruments used were LBC_RED (i and z band) and LBC_BLUE (r band) (Giallongo et al. 2008). Those cameras have four 2048 × 4608 pixel chips each, a pixel scale of 0.23 arcsec and a field of view of about 24×25 arcmin^2. A single chip covers roughly 17×8 arcmin^2.

Total exposure times per filter for the LBT data are between 360 and 720 s, depending on the object. Single exposures were integrated for 180 s regardless of the filter in use.

3.2 Spectroscopic observations

We obtained long-slit spectroscopic data for 14 clusters with ACAM during the visitor mode WHT runs listed in Section 3.1.1, plus one cluster as part of a WHT service programme in 2014 June (PI: Buddendiek). Targets were selected for the spectroscopic observations either if they appeared to be very rich, at very high redshift or if they seemed relaxed due to a single very bright BCG. Integration times varied between 600 and 1100 s per exposure, which results in total integration times between 1800 and 3300 s per target. In all cases, we employed the V400 grating and the G495 filter, which provides a wavelength range from 4950 Å to 9500 Å and 3.3 Å pixel^{-1}. The slit width is 1.0 arcsec, corresponding to a resolution of $R = 570$ at a wavelength of $\lambda = 7500$ Å. For three clusters, the spectra are too noisy and no redshift could be estimated. We generally placed the slit on top of the BCG and if possible oriented it such that other cluster members were visible through the slit as well.

3.3 Data reduction and calibration

The WHT and LBT data are reduced using the GUI version of the THELI[3] pipeline (Erben et al. 2005; Schirmer 2013). We apply bias subtraction, flat-field correction, and superflat field correction. Exposures are co-added and later convolved with a Gaussian kernel to have approximately the same resolution in all bands for photometric measurements.

We calibrate the photometry by fitting the function

$$\mathrm{mag}_{\mathrm{SDSS}} - \mathrm{mag}_{\mathrm{m}} = \mathrm{C}_{\mathrm{SDSS}} \times \mathrm{CT} + \mathrm{ZP} \quad (1)$$

---

[3] http://www.astro.uni-bonn.de/~theli/index.html

to field stars. $\mathrm{mag_m}$ is the measured magnitude, $\mathrm{mag_{SDSS}}$ the corresponding SDSS magnitude, CT the colour term and ZP the magnitude zero-point. $\mathrm{C_{SDSS}}$ is the SDSS colour we use for calibration, either $r - i$ (r- and i-band calibration) or $r - z$ (z-band calibration). After correcting magnitudes with the zero-points, we do not apply a colour correction but work in the instrumental system instead. Every single field is corrected independently. The data reduction for WHT and LBT data is performed in the same way.

In order to determine the limiting magnitude of a co-added image we use

$$m_{\mathrm{lim}} = \mathrm{ZP} - 2.5 \log \left(5 \sqrt{N_{\mathrm{pix}}} \sigma_{\mathrm{sky}}\right), \tag{2}$$

where N_{pix} is the number of pixels within a circle with a radius of 2.0 arcsec and σ_{sky} is the variation of the sky background noise (see Erben et al. 2009). This gives the 5σ detection limit. We find the mean limiting magnitudes of the WHT images to be $r_{\mathrm{lim}} = 23.81$ mag, $i_{\mathrm{lim}} = 23.42$ mag and $z_{\mathrm{lim}} = 22.64$ mag. We also measure the seeing as the full width at half-maximum (FWHM) and find the median seeing $\mathrm{FWHM}_r = 0.95$ arcsec, $\mathrm{FWHM}_i = 0.82$ arcsec, and $\mathrm{FWHM}_z = 0.82$ arcsec. For the LBT data we find $r_{\mathrm{lim}} = 24.52$ mag, $i_{\mathrm{lim}} = 24.95$ mag, $z_{\mathrm{lim}} = 23.63$ mag, and $\mathrm{FWHM}_r = 0.77$ arcsec, $\mathrm{FWHM}_i = 0.92$ arcsec, $\mathrm{FWHM}_z = 0.77$ arcsec.

The spectra are also bias subtracted, flat fielded and then extracted. For the further reduction we use IRAF (Tody 1993). We extract the spectra using the task `apall`. Furthermore, wavelength and flux calibration are performed with the tasks `identify`, `dispcor`, and `calibrate` using skylines and standard star observations.

3.4 Sunyaev–Zel'dovich data

To obtain cluster mass estimates, we targeted a sub-sample of 21 targets with the Combined Array for Research in Millimeter-wave Astronomy to measure the SZE signal, which has been found to correlate with mass with small intrinsic scatter, both from simulations (e.g. da Silva et al. 2004; Motl et al. 2005; Stanek et al. 2010) and observations (e.g. Bonamente et al. 2008; Planck Collaboration XI 2011; Marrone et al. 2012; Planck Collaboration III 2013).

The SZE data for 20 of those clusters were obtained using the eight 3.5-m telescopes of CARMA in the SH and SL configurations.[4] For these configurations, six telescopes are grouped in a compact central array and two on outlying pads. The long baselines resolve out the cluster signal and yield uncontaminated measurements of point sources, which can then be subtracted from the short baseline data. We used the CARMA wideband correlator with 8 GHz of correlation bandwidth. Observations were carried out in the 30 GHz band and integration times were planned to be 8 h for each cluster. Due to various reasons the 8 h were not always reached. The exact integration times can be found in Table B2. The CARMA programme numbers are `c0734`, `c0734Z` (both PI: Schrabback) and `c0934` (PI: Plagge). Those targets were selected because they appeared to be the richest or most distant objects in the sample. Additionally, we also have been granted director's discretionary time for the target ClG-J122208.6+422924 (`cx389`, PI: Buddendiek). This data set was recorded using an antenna configuration different from the SL and SH configurations. All 3.5m-antennas were grouped in a compact array and the 6-m and 10-m antennas are used for long baselines.

The first 20 targets were selected after an initial optical analysis because they appeared to be either the richest, the most X-ray luminous or the highest redshift ones. One should note that at that time the optical campaign was not complete yet. The last of the 21 targets was selected after the optical analysis had been completed and it had a measured spectroscopic redshift greater than 1, which is the highest in the whole sample.

4 OPTICAL DATA ANALYSIS

4.1 Spectroscopic redshifts

After extracting the spectra, we use the IRAF task `fxcor` (Fitzpatrick 1993) in order to cross-correlate them with the absorption line template spectrum `fabtemp97` and the emission line template spectrum `femtemp97`. This yields the redshift estimates. In order to find the uncertainty `fxcor` fits a Gaussian to the correlation peak and we then take the half-width at half-maximum as the redshift error. Visually identified lines and features can be found in Table 1.

The spectra are mainly low S/N spectra due to very faint targets. The redshifts are mostly estimated using absorption features like the Ca K+H doublet, thus the errors for the redshifts are comparably high (≈0.5 per cent). Individual errors can be found in Table 1.

In our analysis, we also include the already known redshifts of twelve galaxy clusters. Those were taken either from the SDSS Data Release 10 (Ahn et al. 2014) or from other independent discoveries. In one of those cases (ClG-J131339.7+221151), a spectrum from the SDSS was available but no reliable redshift has been estimated ($z_{\mathrm{SDSS}} = 1.000 \pm 3.359$); we downloaded the already reduced and extracted spectrum and estimate the redshift ourselves. All redshifts used in this study are listed in Table 1, which also includes additional information.

4.2 Red sequence finding and redshift estimation

We derive empirical red sequence models in $r - i$, $i - z$, and $r - z$ using 12 clusters from the WHT sample with known spectroscopic redshifts. For this we use the colour–magnitude diagram of galaxies within the inner 50 arcsec around the BCG. Again, we employ a constant angular radius and not a physical one given the small change in the angular diameter distance between $z = 0.6$ and 0.9.

Within this radius, we fit a linear function of galaxy colour versus magnitude as a red sequence yielding slope and offset. We then assume that red sequence slope and offset change linearly with redshift and thus fit both as a linear function of z. Using these fits we can derive an empirical red sequence model for every redshift in the range $0.5 \lesssim z \lesssim 0.9$. Additionally, we extrapolate these models to $z = 0.4$ and 1.0. We are aware that the red sequence slope and off-set do not in general vary linearly with redshift. Nevertheless, this assumption provides a good approximation given the redshift range and filter choice. The models created can be used for both the WHT and the LBT sample, because their filter sets are fairly similar; for the service observations in 2010, we create models in the same way but using different clusters, due to the different filters used. The clusters used to create the models for the WHT and LBT samples spread almost evenly in the redshift range between $z \approx 0.55$ and 0.9. For the models for the WHT service observations, we only have redshifts available between $z \approx 0.6$ and 0.8. Later on in this section, we will find these models to be sufficient for our purposes (see Fig. 2).

---

[4] Configurations of the eight 3.5m (formerly SZA) antennas of CARMA: SH is a hybrid configuration with two antennas on outlying pads. SL is a similar configuration, optimized for low-declination targets.

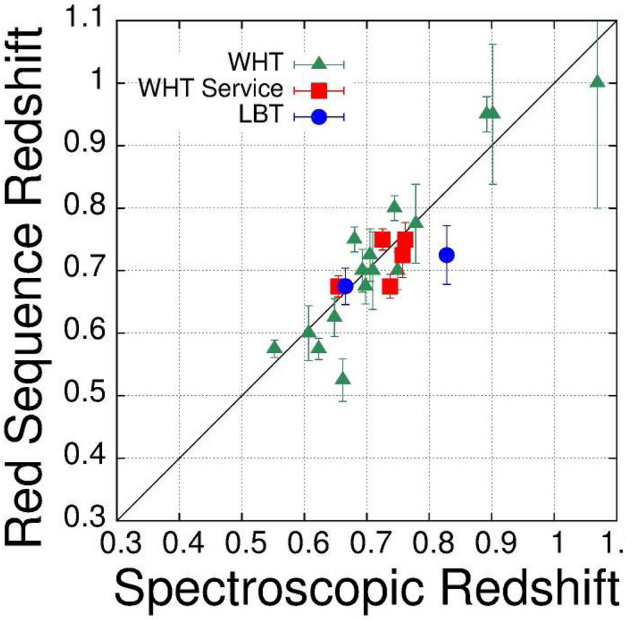

Figure 2. Comparison of spectroscopic versus red sequence redshifts of galaxy clusters. Error bars represent statistical errors and photometric errors, which originate from the photometric calibration. The black line shows the one on one relation. No systematic bias seems to be present.

We create the galaxy catalogue with aperture photometry in dual image mode, using the i band as the detection image. Due to the homogenized point spread function (PSF), we suppress background noise and thus underestimate the photometric errors. To avoid this issue, we run SExtractor (Bertin & Arnouts 1996) again on the unconvolved images and use those magnitude errors. Nevertheless, we find that we still underestimate the photometric errors due to multiple reasons. For example, during the reduction we resample the images to a new pixel grid, which correlates the background noise. This has a similar effect as the PSF homogenization. We also use aperture photometry, which can lead to additional photometry errors, in case of a not completely homogeneous PSF in all three filters. In order to account for this, we take the photometric errors from SExtractor to be twice as large as the original value. A factor of 1.3 is due to noise correlations, the remaining due to uncertainties arising from the limitations in the PSF homogenization. This is performed by assuming Gaussian PSFs and by quantifying the PSF using the flux radius, which is not a complete description of the PSF. In the end this results in a total correction factor of 2. Using the newly created models, we find the red sequence and the corresponding redshifts by taking the following steps, which are similar to the approach used in High et al. (2010):

First, we identify the BCG in the colour image. We then use all galaxies, which are within a given radius R around the BCG. Additionally, we only take galaxies with an S/N larger than 6 in the i band into account. Between redshifts 0.4 and 1.0, we proceed in steps of $\Delta z = 0.025$ and use the corresponding red sequence model to look for galaxies in the catalogue which lie within a certain error range in colour, Δc, from the red sequence lines in all three colours. Here, we also use galaxies even if they only fall within that range, when taking their magnitude errors into account. Although we only use the inner parts around the cluster centre we are still affected by fore- and background galaxies, which are contaminating the colour–magnitude diagram. In order to avoid false detections through these galaxies, we determine and subtract an average red sequence background. Since the ACAM field of view is fairly small, we use about 100 apertures in the public CFHTLenS catalogue (Erben et al. 2013; Hildebrandt et al. 2012), using the same cuts as for the actual galaxy catalogues in order to estimate the mean red sequence object density. After normalizing by the projected area and subtracting the background, we choose the redshift bin which contains the most galaxies to be our red sequence redshift estimate. The error range Δc, and the aperture radius R are free variables, which can be chosen arbitrarily. We explore the parameter space spanned by those two parameters, looking for the combination which recovers the known spectroscopic redshifts best. Although we vary the radius R for each cluster, we find that the best choice for all the WHT objects is $R = 1.25$ arcmin and $R = 0.76$ arcmin for all the LBT targets. While looking for the red sequence for every cluster candidate, we maximize the signal by varying Δc in discrete steps between 0.01 and 0.2. In the end for each cluster we pick the value, which leads to the strongest signal. A typical value here is $\Delta c = 0.08$.

We plot the estimated spectroscopic redshifts against their measured photometric counterparts for the best configuration of R and Δc. As can be seen in Fig. 2, no systematic bias is present, and on average the red sequence redshift estimates agree with the spectroscopic ones. Thus, we decide not to calibrate the estimates further.

The comparison with the spectroscopic sample shows that the models work fine as we find $\sigma_z = 0.037$, which we define as

$$\sigma_z = \sqrt{\frac{1}{N}\sum\left(\frac{z_{\rm spec} - z_{\rm phot}}{1 + z_{\rm spec}}\right)^2}, \tag{3}$$

where N is the number of galaxy clusters with a known spectroscopic redshift and $z_{\rm spec}$ and $z_{\rm phot}$ is their corresponding spectroscopic or red sequence redshift.

We also try building analytical models from Bruzual & Charlot (2003), taking into account filter curves, quantum efficiency, and reflection curves of all optical elements inside the telescope, but we found that, especially at the low- and high-redshift regions in our sample, the redshift estimation failed completely. These models apparently do not match the observed galaxy distribution over the whole redshift range. Already Hildebrandt et al. (2010) showed that photometric redshift codes, which are tested on a suitable training sample, usually work best while using empirical models. In the end we decided to use the empirical models rather than the analytical ones. A colour image of a typical cluster, a background subtracted histogram of possible red sequence members, the red sequence corresponding to the photo-z estimate and also the number counts (Section 4.3) can be seen in Fig. 3.

We estimate statistical errors from bootstrapping the whole galaxy catalogue and estimating the redshift several thousand times. To the standard deviation of the distribution, which is the statistical error, we quadratically add the magnitude zero-point error, which gives a fair estimate of the photometric error, and take this as the red sequence redshift uncertainty. We check if this is indeed a fair representation of the true uncertainty by computing the standard deviation, Δz, of $z_{\rm spec} - z_{\rm phot}$ and comparing it with the mean redshift error $\langle \Delta z \rangle$. We find $\Delta z = 0.048$ and $\langle \Delta z \rangle = 0.044$. This means that on average Δz is a good representation of the true redshift uncertainty.

4.2.1 *Defining a detection*

After running our red sequence finder on the data of all 48 cluster candidates, which have three-band imaging, we define a detection using two criteria.

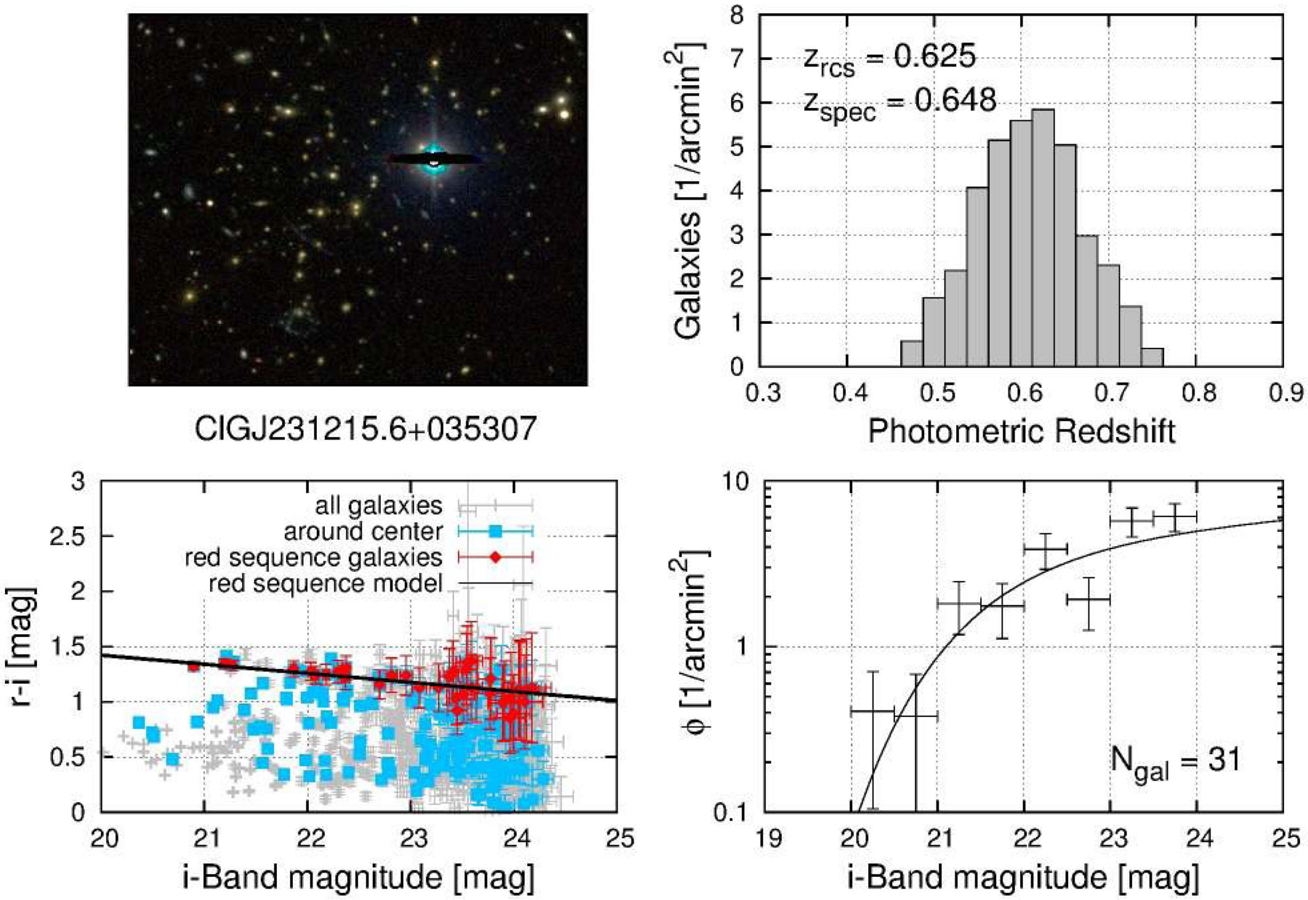

Figure 3. This figure shows the output of the red sequence analysis for one cluster, ClG-*J*231215.6+035307. The top-left panel shows a colour image of the inner parts of the cluster. In the top-right panel, we show the number of galaxies around the cluster centre, which coincide with the red sequence models as a function of redshift. Here the peak lies at $z = 0.625$. The bottom-left panel shows a colour–magnitude diagram. Grey points are all galaxies in the field, blue points are galaxies within 1.25 arcmin of the centre and red points are red sequence galaxies. The black line shows the red sequence for $z = 0.625$. Finally, the bottom-right panel shows the *i*-band number counts of the cluster members, shown in the figure to the left. The black line is the best Schechter function fit. The fact that the number counts do not start to decrease at fainter magnitudes suggests that we do not suffer from significant incompleteness issues.

(i) The object shows a peak in the red sequence histogram (see Fig. 3, top-right panel).

(ii) In the three-colour image, we can visually find an overdensity of galaxies, which have the same colour.

If both these criteria are true, we consider this a detection and continue the analysis. If only one or none are true, we stop the analysis after the red sequence finding and consider this a non-detection. From the 48 cluster candidates, we detect 44 according to these criteria. The three previously known clusters are detected as well.

4.3 Richness estimates

We define the richness N_{gal} to be the number of cluster galaxies within 0.5 Mpc around the BCG, which are brighter than some characteristic magnitude of the cluster luminosity function. We will now describe the procedure to estimate N_{gal}.

Once the red sequence redshift was estimated, we created new catalogues with all galaxies which were detected as a red sequence member in all three colours at this redshift. For the aperture radius r, we now choose 0.5 Mpc. The galaxies are divided in magnitude bins of size 0.5 mag between 19th and 24th magnitude in the i band and normalized to the area. Again, a background is estimated from CFHTLenS and subtracted. We then fit a Schechter function (Schechter 1976) normalized to projected area rather than volume to the data

$$\phi(m)\,\mathrm{d}m = 0.4\,\ln 10\,\phi^{*} 10^{-0.4(m-m^{*})\cdot(\alpha+1)} \times \exp[-10^{-0.4(m-m^{*})}]\,\mathrm{d}m. \quad (4)$$

For the fit we keep α fixed to -1.1, which has been shown to be robust for rich clusters (e.g. Paolillo et al. 2001). Furthermore, we assume passive stellar evolution and use the stellar population synthesis models from Bruzual & Charlot (2003) with the Padova stellar evolution models (Bertelli et al. 1994) and the initial mass function by Chabrier (2003) to fix m^{*} for every redshift. In the end, we only fit the normalization ϕ^{*}. Subsequently, we integrate the Schechter function up to $m^{*} + 2$. After multiplying the result with the projected area this gives us our richness estimate, N_{gal}. An example of such a measured function can be found in the bottom-right panel of Fig. 3.

We estimate statistical errors for the richness by bootstrapping the cluster member sample and repeating the whole estimation procedure several thousand times. We then quadratically add the Poissonian error and take this as the total uncertainty in richness. For comparison, we also estimate the richness of a cluster by counting the red sequence galaxies that are brighter than $m^{*} + 2$ and call this

$N_{\rm count}$. Here, we take the Poissonian error as the uncertainty. For the further analysis we use only the $N_{\rm gal}$ estimates, because we expect them to be more robust.

Redshifts, richnesses and other properties as well as comments concerning the data and the analysis can be found in Table B1.

4.4 Discussion of the results from the optical data

With our analysis, we confirmed 44 galaxy clusters at redshifts between $0.5 \lesssim z \lesssim 1.0$. Additionally, we conducted the analysis for three previously known clusters in order to have a calibration sample. The cluster richnesses within 0.5 Mpc vary between 3 and 46. We summarize all measured quantities in Table B1. One column in this table lists problems that occurred during the analysis. Those problems were poor observing conditions like high airmass, cloud coverage etc. which lead to considerable systematic uncertainties. Furthermore, the galaxy redshift distribution in the histograms like the one shown in Fig. 3 does not always have a clear peak, sometimes it is bimodal. Additionally, the Schechter function fit can fail, which can for example be caused by a poor redshift estimate due to a faint cluster. An example for this is ClG-*J*094742.3+351742. From the fit we find $N_{\rm gal} = 20 \pm 4$, which does not agree with the counted estimate of $N_{\rm count} = 2 \pm 1$. Poor data in one or more bands can also lead to poor richness estimates. The *r* band of ClG-*J*144847.4+284312 for example is much shallower than the rest of the data, because it was observed in bright time. Due to this we overestimate the background in this field, which leads to the low values in $N_{\rm gal} = 3 \pm 2$ and $N_{\rm count} = 3 \pm 2$.

The redshift and richness distribution of our sample can be found in Fig. 4. The redshift distribution peaks at $z = 0.75$. We targeted a redshift range of $0.6 \lesssim z \lesssim 1.0$ while cross-correlating RASS and SDSS. In this respect the left-hand panel of Fig. 4 is a confirmation that our approach works indeed. The richness distribution shows a peak between 20 and 30 and then a decreasing trend towards higher richness. The most interesting objects are those at the high richness tail at $N_{\rm gal} > 30$. Nevertheless, all objects in this sample seem to be rare X-ray luminous high-redshift galaxy clusters, which makes them interesting objects for further research.

By inspecting the colour images, 11 clusters with one or more potential strong gravitational lensing features were found. Those clusters and the arc coordinates are listed in Table 2 and corresponding colour images can be found in Fig. 5.

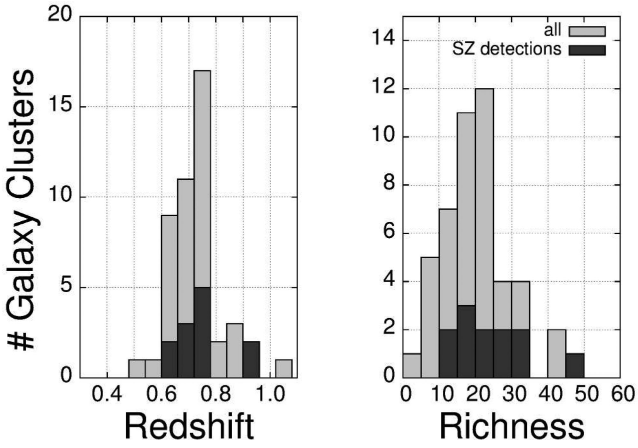

Figure 4. Redshift and richness distribution of all 44 galaxy clusters in our sample and of the three previously known objects. Wherever available we use spectroscopic redshifts. Light grey bars show the whole sample, dark grey bars the SZ-detected clusters only.

Table 2. This table names clusters where potential strong lensing features were found and gives their coordinates.

Object	RA	Dec.
ClG-*J*013710.4−103423	01:37:09.87	−10:34:31.15
ClG-*J*080434.9+330509	08:04:37.90	+33:04:53.49
ClG-*J*083415.3+452418	08:34:16.82	+45:23:24.15
ClG-*J*104803.7+313843	10:48:04.68	+31:38:51.70
	10:48:03.71	+31:38.29.46
	10:48:04.47	+31:39:05.18
ClG-*J*124515.2+245335	12:45:15.25	+24:53:46.61
ClG-*J*142040.3+395509	14:20:37.48	+39:54:48.53
	14:20:38.61	+39:54:52.47
ClG-*J*142138.3+382118	14:21:39.41	+38:21:05.21
ClG-*J*214826.3−053312	21:48:25.77	−05:33.02.26
ClG-*J*231215.6+035307	23:12:16.79	+03:52:38.90
	23:12:16.99	+03:52:12.15
ClG-*J*231520.6+090711	23:15:21.73	+09:07:34.09
	23:15:19.88	+09:07:06.59
RCS2-*J*232727.7−020437	23:27:29.41	−02:03:48.03
	23:27:30.69	−02:04:29.47

Due to the two clusters RCS2-*J*232727.7−020437 and ClG-*J*120958.9+495352 being in both the WHT as well as the LBT sample, we have the possibility to cross-check the results. The red sequence redshifts both agree within 2σ with the spectroscopic redshift. Comparing richness, we see that for ClG-*J*120958.9+495352 the measured values from the WHT sample are, within the error bars, consistent with the ones from the LBT sample (ClG-*J*120958.9+495352: 18 ± 5; 22 ± 5). For RCS2-*J*232727.7−020437 the Schechter function fit did not work for the LBT data and thus the estimate for $N_{\rm gal} = 11 \pm 6$ is very different to the one from the WHT (46 ± 7). This is due to the values we fix the parameters in the Schechter function to. Those apparently do not match the observed data for RCS2-*J*232727.7−020437 in the deeper LBT data.

Six of the clusters in this sample had been discovered independently by Wen, Han & Liu (2012), another four by the *Planck* collaboration (Planck Collaboration XXVII 2015). We marked those clusters in Table B1.

5 SZ DATA ANALYSIS

The SZE signal is quantified in terms of the Compton *y* parameter, the line-of-sight integrated pressure. For scaling with mass, a convenient measure is the integrated Comptonization

$$Y = \int y\, {\rm d}\Omega = \frac{1}{(D_{\rm A})^2} \frac{\sigma_{\rm T}}{m_{\rm e}c^2} \int {\rm d}l \int P(r)\, {\rm d}A, \qquad (5)$$

where Ω is the subtended solid angle of the cluster on the sky, $D_{\rm A}$ is the angular diameter distance, $\sigma_{\rm T}$ is the Thomson cross-section, $P(r)$ is the projected pressure profile and A is a projected physical area. Following Marrone et al. (2012), we quantify the SZ signal in terms of the *spherical* measure

$$Y_{\rm SZ} \equiv Y_{\rm sph}(D_{\rm A})^2 = \frac{\sigma_{\rm T}}{m_{\rm e}c^2} \int P(r)\, {\rm d}V, \qquad (6)$$

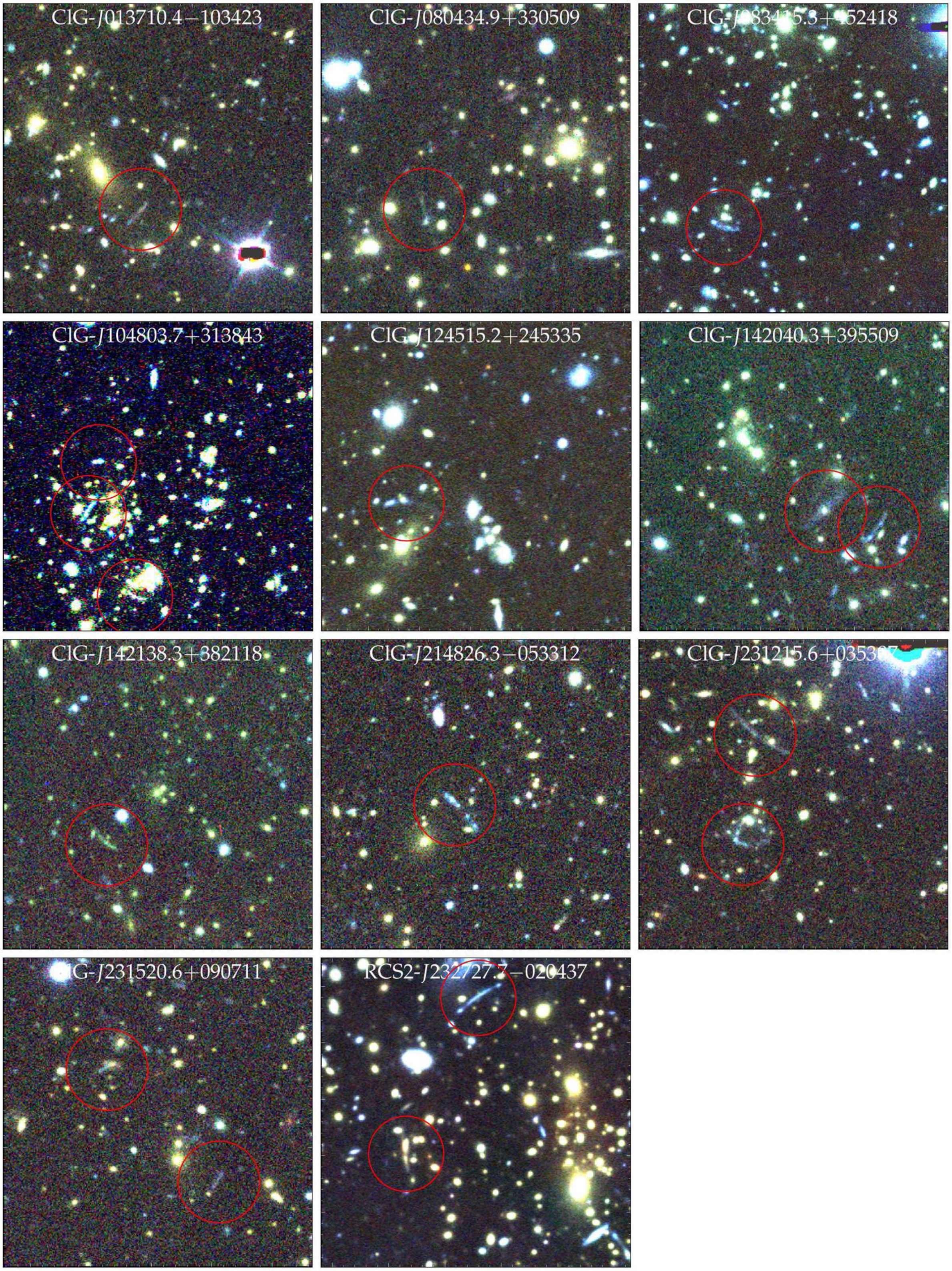

Figure 5. Strong lensing arc candidates. All panels show 75 arcsec × 75 arcsec. Arc candidates are highlighted by a red circle.

where dV is a physical volume element and $P(r)$ is now the pressure as a function of physical radius. Note that we have moved D_A to the left-hand side of the equation to remove the redshift dependence in the SZE measure.

For the pressure as a function of radial distance, we adopt the generalized NFW pressure profile (Nagai, Kravtsov & Vikhlinin 2007), with the functional form

$$P(r) = \frac{P_0}{c_{500}x^{\gamma}(1 + c_{500}x^{\alpha})^{(\beta-\gamma)/\alpha}}, \tag{7}$$

where $x = r/r_{500}$ and $(P_0, c_{500}, \alpha, \beta, \gamma)$ are parameters of the model. For our analysis, we fix $(\alpha,\ \beta,\ \gamma)$ to the best-fitting values of the 'universal pressure profile' (UPP) found by Arnaud et al. (2010).

We reduce the CARMA data using a pipeline similar to the one used in Muchovej et al. (2007), which was adapted for the use with CARMA. We first filter out bad weather errors as well as pointing errors and then apply a gain and flux calibration. For the flux calibration, we use the model of Mars from Rudy et al. (1987). We assume that Mars is a disc of uniform brightness, Fourier transform this disc to the visibility plane and compare it to the measured visibilities. From this comparison, we derive an antenna-specific scale factor, which brings the observations in line with the model. A conservative estimate for the absolute flux calibration uncertainty is ~7 per cent. This results from ~5 per cent uncertainty in the model from Rudy et al. (1987) and ~5 per cent uncertainty from the gain solution of the telescopes.

We carry out a model fit using the pressure profile of Arnaud et al. (2010) to the interferometric data by Fourier transforming the model and comparing it to the data in visibility space. We minimize a χ^2 statistic and estimate the detection significance. If this significance is greater than three we estimate the spherical volume-integrated Comptonization, $Y_{\rm SZ}$. If the significance is less than three, we only give upper limits on $Y_{\rm SZ}$ and the mass. We call these cases non-detections. We estimate r_{500} by forcing $Y_{\rm SZ}$ to be consistent with the $Y_{\rm SZ}$–M_{500} scaling relation of Andersson et al. (2011), which effectively means we are fitting only to integrated Comptonization (or equivalently, mass) from which r_{500} is directly given. We use the scaling relation with a fixed slope of 1.79. The positions and peak fluxes of point sources detected in the long-baseline image are included in the fit (rather than subtracted in the visibility-plane), and marginalized over in determining $Y_{\rm SZ}$.

In addition to the statistical errors in the fit there are further sources of uncertainty. First, there is intrinsic scatter in the M–$Y_{\rm SZ}$ scaling relation, for which we assume a 21 per cent intrinsic scatter in mass consistent with Andersson et al. (2011). We add this scatter in quadrature to the statistical errors of the fit as it assumes that the clusters follow the scaling relation exactly. In addition, it is important to realize that this scaling relation has been calibrated via the M–$Y_{\rm X}$ scaling relation, which itself was calibrated empirically using weak lensing data at much lower redshifts only (Vikhlinin et al. 2009). Given the high-redshift range of our clusters, any deviation from the assumed self-similar redshift evolution would lead to a systematic bias in the derived masses. So far, Jee et al. (2011) present the only weak lensing study for a large cluster sample at high redshifts. Their analysis suggests a possible evolution in the $M - T_{\rm X}$ scaling relation until $z \sim 1$ in comparison to self-similar evolution at the 20–30 per cent level. To be conservative, and accounting for the in comparison to Jee et al. (2011) slightly lower redshift range of our clusters ($z_{\rm median} = 0.725$), we therefore adopt an additional 20 per cent systematic uncertainty in the mass scale. Andersson et al. (2011) use a cosmology slightly different to ours, introducing another systematic bias of about 5 per cent in mass, which is however negligible compared to the statistical errors.

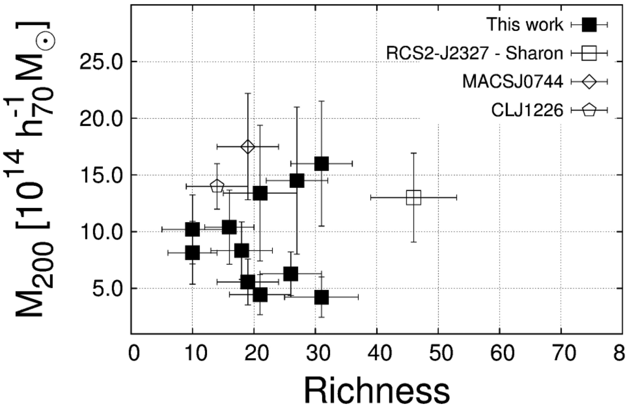

Figure 6. We show mass estimates as a function of richness. The solid points are SZ masses from this study. The open symbols are masses from previous studies. The masses for RCS2-*J*232727.7−020437 were determined from $Y_{\rm SZ}$ given in Sharon et al. (2015), which was measured from CARMA data. For MACS074452.8+392725 the mass estimate is taken from Umetsu et al. (2014), which is a weak lensing mass estimate. Jee & Tyson (2009) measure a weak lensing mass for ClG*J*1226+33. The error bars in mass for objects from this work include the 21 per cent scatter from the scaling relation from Andersson et al. (2011) but not the 20 per cent systematic error due to the high-redshift mass calibration (see Section 5).

For ClG-*J*122208.6+422924, which was observed in a different configuration, we used the 6-m and 10-m antennas to search for point sources and the 3.5-m antennas to estimate $Y_{\rm SZ}$. We analysed about 4 h of these data but could not detect the cluster. Half of the data had only been observed at half the normal bandwidth. From the 21 clusters analysed we detect 11. For those we estimate M_{500} according to the scaling relation. Furthermore, using the mass–concentration relation from Duffy et al. (2008) we can convert this to M_{200}. Again, for the non-detections, we only determine upper limits. In Fig. 6, we show how the masses from the SZ data scale with our richness estimates. Additionally, we also show masses which were already known for RCS2-*J*232727.7−020437, MACS074452.8+392725, and ClG*J*1226+33. M_{200} for RCS2-*J*232727.7−020437 was determined from the value given for Y_{SZ} in Sharon et al. (2015), which had been measured from CARMA data. We estimate $M_{200} = (11.3 \pm 3.9) \times 10^{14}\,h_{70}^{-1}\,{\rm M}_\odot$ using the cosmology adopted in our work; the given uncertainty is dominated by the uncertainties in the scaling relation. For MACS074452.8+392725, we use the weak lensing mass estimate from Umetsu et al. (2014). Also, Jee & Tyson (2009) estimate a weak lensing mass for ClG*J*1226+33. The mass estimates for MACS074452.8+392725 and ClG*J*1226+33 use different techniques than we do, which means that they do not necessarily measure the same mass as our SZ estimate.

In the plot there is only a rough relation between mass and richness visible; one can see large scatter among the data. This is expected due to comparably short integration times, the assumptions we make while determining the masses but most importantly due to the large intrinsic scatter between mass and richness (e.g. Angulo et al. 2012). We also find that our M_{500} estimates range mostly between 3 and 9 $\times\ 10^{14}\,h_{70}^{-1}\,{\rm M}_\odot$ at redshifts of $0.6 \le z \le 0.9$. That we only find these high masses is due to a selection effect; the less massive clusters could not be detected at $>3\sigma$ in the SZ data, while using only these comparably short integration times.

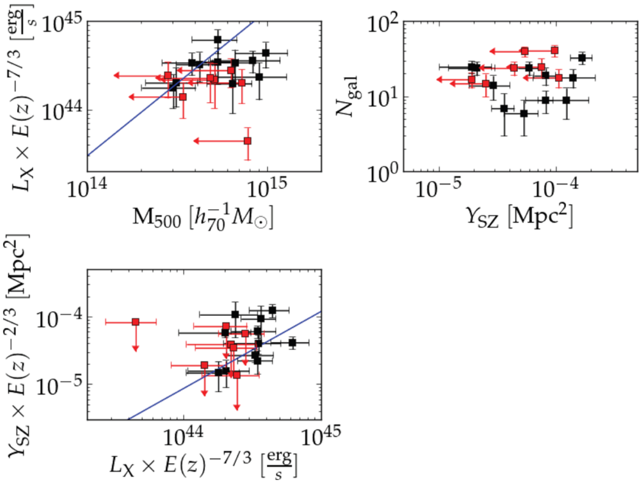

Figure 7. We present scaling relations comparing the *ROSAT* X-ray luminosity L_X, the integrated Comptonization parameter Y_{SZ} from the CARMA data, the SZ-inferred galaxy cluster mass M_{500}, and the cluster richness N_{gal}. The black points show the CARMA detections, the red points the CARMA non-detections, and the corresponding 3σ upper limits. The blue lines show corresponding relations from Arnaud et al. (2010). We assume self-similar evolution in order to compare the data to the scaling relations from Arnaud et al. (2010). For a detailed discussion please see Section 5.

The objects that have not been detected with CARMA are in most cases not particularly rich in the optical or were only integrated for a short amount of time. There are two exceptions. One of these is ClG-*J*142040.3+395509, for which we find a point source at the BCG position, which can potentially cancel the SZ-signal. Due to a flagged antenna, we do not have enough long baselines to properly measure the flux of this source. This could explain the apparent strong SZ-peak, with an offset of about 2 arcmin from the BCG position. The other one is ClG-*J*095416.5+173808, which is optically rich, but not detected. As we already explained before, there is a large scatter in the mass–richness relation, so this could mean that ClG-*J*095416.5+173808 shows a strong richness while not being massive, which would result in a faint SZ signal.

In Fig. 7, we show the M_{500}–L_X, the L_X–Y_{SZ}, and the Y_{SZ}–N_{gal} scaling relations. The blue lines show the corresponding M_{500}–L_X and L_X–Y_{SZ} relations from Arnaud et al. (2010). In order to compare the data to those relations, we assume self-similar evolution, which depends on the self-similar evolution factor $E(z) = H(z)/H_0 = \sqrt{\Omega_m(1+z)^3 + \Omega_\Lambda}$ (in this form it is only true for flat cosmologies). We plot both, the CARMA detections, as well as the non-detections (denoted in red) using their 3σ upper limits. The measured M_{500}–L_X and the L_X–Y_{SZ} relations agree well with the results from Arnaud et al. (2010). The non-detections seem to have a preferentially lower L_X than the detections. When comparing N_{gal} to Y_{SZ} we find no clear trend, as already discussed for Fig. 6. We do not attempt to compare the mass–richness or Y_{SZ}–richness relations to previous works, due to differences in the definition of richness between studies.

All results from the CARMA SZ observations can be found in Table B2. In addition to the CARMA data, we also check if the clusters observed with CARMA can be found in data from *Planck*. A detailed description of this and postage stamps of the CARMA and *Planck* SZ-maps are given in the appendix.

6 ARE THERE GALAXY CLUSTERS TOO MASSIVE COMPARED TO PREDICTIONS FROM ΛCDM?

Using M_{200} estimated from the SZ data, we can check for 11 clusters if they are too massive for our current structure formation paradigm. For this we use the fitting formula given in Mortonson et al. (2011) for upper mass limits as a function of redshift and survey size in a flat ΛCDM cosmology. One limitation here is that we do not test the whole sample but every cluster individually. We do not know the exact area which has been used for our cluster detection, due to our selection procedure. Nevertheless, we can calculate a lower limit for the area. For this we use all galaxies from the SDSS DR8, which includes the complete SDSS imaging data, with `psfMag_i` < 13 and all objects from the RASS faint source catalogue. We grid both samples and compute the overlapping area as the sum of cells, which contain at least one object of each survey. This estimate does strongly depend on the cell size and does not converge. In order to find a lower limit on the area used, we vary the cell size and check how many of the 44 clusters are within the overlapping area. The smallest cell size for which we still find all clusters within the overlap is $0.7 \times 0.7\,\mathrm{deg}^2$. For this configuration, we find the area to be $\approx$10 000 deg^2. This estimate is, as mentioned before, only a lower limit and it does not take variations in sensitivity in the SDSS and RASS into account. Thus, we only provide this area estimate to put our findings into a cosmological context. We also test if our sample selection is sensitive to the exposure time in RASS. We find the lowest exposure time of a cluster in the sample to be $\approx$350 s. Areas in RASS with exposure times greater or equal to these 350 s correspond to about 80 per cent of the total RASS area. We plot the cluster masses against redshift in Fig. 8. Additionally, the masses of three clusters from previous studies are plotted (see

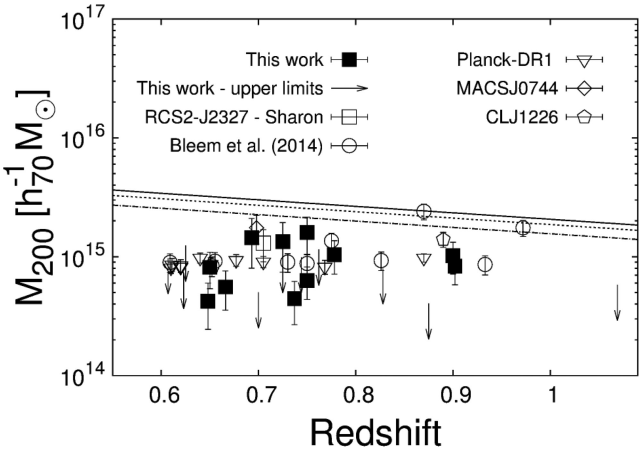

Figure 8. The solid line shows the 99 per cent confidence mass limit as a function of redshift for a flat ΛCDM universe and the survey size of *Planck*. The dotted line shows the same limit for a survey size of 10 000 deg^2, which corresponds to the survey size in this work. The dash–dotted one shows the corresponding limit for the SPT 2500 deg^2 survey. To compute these lines, we use the fitting formula from Mortonson et al. (2011) and acknowledge the fact that this gives too strict limits. The solid points show the masses estimated in this study. The other symbols represent masses from previous studies. Arrows indicate the upper limits we find in CARMA for non-detected clusters. We find no tension with the ΛCDM model. The open circles are the 10 most massive clusters between $0.6 < z < 1.0$ from Bleem et al. (2015), the triangles with the tip down show the 10 most massive clusters in this redshift range in the *Planck* SZ sample (Planck Collaboration XXIX 2014).

Section 5). Furthermore, we take the 10 most massive clusters at redshifts $0.6 < z < 1.0$ from Bleem et al. (2015)[5] and also from *Planck* (Planck Collaboration XXIX 2014),[6] determine their M_{200} as described above and plot them as well. The masses we find for both of these samples are comparable to ours. Considering that we use the most massive ones from that study, this might again be an indication of the massive and extreme nature of our cluster sample.

As visible in Fig. 8, we find no significant tension between our clusters and the current cosmological standard model. The clusters from Bleem et al. (2015) and from *Planck* were found by different surveys using a different selection function. Thus, from Fig. 8 we should not infer possible tension for those clusters. We are aware that Hotchkiss (2011) showed that the fitting formula we use is too strict, but since none of the objects is in strong tension, the method from Mortonson et al. (2011) is sufficient for our purposes.

Only a sub-sample is tested here and ideally we would like to achieve mass estimates for more clusters than these 11, preferably for those with the highest N_{gal}, since this should be a rough indication for the mass.

7 NOTES ON INDIVIDUAL CLUSTERS

After this summary of the general data, we will now focus on the most notable objects in the sample, which are either high-redshift clusters, very rich clusters in the optical or very massive clusters according to their SZ signal. Those clusters are the most interesting targets for further and deeper follow-up observations, in order to determine their masses and other interesting properties.

7.1 RCS2-*J*232727.7−020437

We can confirm this object to be a very rich cluster. The measured photometric redshift $z_{\text{phot}} = 0.725 \pm 0.042$ agrees well with the known spectroscopic one, $z_{\text{spec}} = 0.705$ (Menanteau et al. 2013). The richness of 46 ± 7 (WHT) is the largest in the sample, as expected from its high mass. However, as we will see later on, there are comparable clusters in our sample. Its mass has been estimated before. For example Gralla et al. (2011) find $M_{500} = (6.2 \pm 0.8) \times 10^{14}\, h_{70}^{-1}\, \mathrm{M}_{\odot}$. Hasselfield et al. (2013) estimate masses from ACT data and use different ways to fix their *Y*–*M* scaling relation. This leads to different mass estimates for RCS2-*J*232727.7−020437. The results from using what they call a UPP scaling relation is $M_{500} = (9.4 \pm 1.5) \times 10^{14}\, h_{70}^{-1}\, \mathrm{M}_{\odot}$, which is their lowest estimate. Their largest value arises from using a scaling relation determined with dynamical masses. With $M_{500} = (14.9 \pm 3.0) \times 10^{14}\, h_{70}^{-1}\, \mathrm{M}_{\odot}$ this is about 50 per cent larger than the UPP value. From the Y_{SZ} given in Sharon et al. (2015), we estimate $M_{500} = (8.1 \pm 2.3) \times 10^{14}\, h_{70}^{-1}\, \mathrm{M}_{\odot}$. This agrees well with the value from Gralla et al. (2011) and within 1σ with the UPP mass from Hasselfield et al. (2013).

7.2 ClG-*J*095416.5+173808

ClG-*J*095416.5+173808 has a measured photometric redshift of $z_{\text{phot}} = 0.725 \pm 0.047$, which scatters 2σ low compared to $z_{\text{spec}} = 0.828$ (Nastasi et al. 2014). The richness of $N_{\text{gal}} = 40 \pm 6$ is comparable to the one of RCS2-*J*232727.7−020437. We do not detect this object with more than 3σ in CARMA.

7.3 ClG-*J*104803.7+313843

This object is located at $z_{\text{phot}} = 0.750 \pm 0.047$ and has a richness of 31 ± 5. Its redshift appears to be slightly higher than the one measured for RCS2-*J*232727.7−020437. The existence of at least two potential arcs indicates a high mass, which is confirmed from the SZ observations, where we estimate $M_{200} = (16.0 \pm 5.5) \times 10^{14}\, h_{70}^{-1}\, \mathrm{M}_{\odot}$. This makes it one of the most massive systems known at high redshift.

7.4 ClG-*J*120958.9+495352

We discovered ClG-*J*120958.9+495352, which has a spectroscopic redshift of $z_{\text{spec}} = 0.902$ and a measured red sequence redshift of $z_{\text{phot}} = 0.950 \pm 0.112$ (WHT). The richness within 0.5 Mpc was measured to be 18 ± 5 (WHT). Due to its large distance, we cannot probe the luminosity function down to faint magnitudes. Based on the RASS count rate this is the most X-ray luminous cluster discovered by our programme with $L_{\mathrm{X}} = (20.3 \pm 6.2) \times 10^{44}\,\frac{\mathrm{erg}}{\mathrm{s}}$. In addition to the findings from the optical data, we estimate its SZ-mass to be $M_{200} = (8.3 \pm 2.5) \times 10^{14}\, h_{70}^{-1}\, \mathrm{M}_{\odot}$.

7.5 ClG-*J*122208.6+422924

ClG-*J*122208.6+422924 is the object with the highest measured red sequence redshift in our sample ($z_{\text{phot}} = 1.000 \pm 0.200$). The large error arises from the fact that only very few cluster members are visible, and those have an average *i*-band magnitude of $i \approx 24.1$, which is very close to the detection limit. The measured spectroscopic redshift is somewhat larger with $z_{\text{spec}} = 1.069$, which was measured from the two brightest cluster members, and both spectra show a clear break at the corresponding 4000 Å position. This makes the object by far the highest redshift one in the sample. Nevertheless, the two brightest cluster galaxies are detected in the SDSS, which given their high-redshift is very rare and might indicate a high mass for those galaxies. We do not detect this object in 4 h of CARMA data but measure a 3σ upper mass limit $M_{500} < 3.8 \times 10^{14}\, h_{70}^{-1}\, \mathrm{M}_{\odot}$.

7.6 ClG-*J*133732.5+195827

This cluster has a redshift of $z_{\text{phot}} = 0.900 \pm 0.106$, but it was observed at a high airmass, which might have affected the data. It does show a strong SZ signal, and considering its possibly high redshift its mass of $M_{200} = (10.2 \pm 3.0) \times 10^{14} h_{70}^{-1}\, \mathrm{M}_{\odot}$ is extraordinarily high. The optical colour image shows only a few very red galaxies, and we measure its richness as $N_{\text{gal}} = 10 \pm 5$.

7.7 ClG-*J*135345.0+432905

ClG-*J*135345.0+432905 shows a very strong SZ signal and with $M_{200} = (13.4 \pm 6.0) \times 10^{14} h_{70}^{-1}\, \mathrm{M}_{\odot}$ it is among the most massive clusters in the CARMA sample. It has no spectroscopic redshift but we measure the red sequence redshift to $z_{\text{phot}} = 0.725 \pm 0.024$. Its richness is $N_{\text{gal}} = 21 \pm 6$.

7.8 ClG-*J*142040.3+395509

This cluster has a spectroscopic redshift of $z_{\text{spec}} = 0.607$ (Bayliss et al. 2011) and shows a richness of $N_{\text{gal}} = 25 \pm 5$. From serendipitous *Chandra* observations, we conducted an X-ray analysis, which

---

[5] http://pole.uchicago.edu/public/data/sptsz-clusters/index.html

[6] http://pla.esac.esa.int/pla

can be found in Appendix A. This analysis shows a gas temperature of about 8^{+3}_{-2} keV, which indicates a high mass. Also, Bayliss et al. (2011) find several strong lensing features and a high velocity dispersion of $\sigma_v = 1095^{+86}_{-175}\ \frac{\mathrm{km}}{\mathrm{s}}$. Oguri et al. (2012) use weak and strong gravitational lensing to measure its virial mass, which, adapted to the cosmology we use, is $M_{\mathrm{vir}} = 10.77^{+3.59}_{-2.88} \times 10^{14}\,\mathrm{M}_{\odot}$. Still, we did not detect this cluster at more than 3σ using CARMA. A possible explanation is a point source we find at the BCG position. This source could counter act the SZ signal and thus we would not detect the cluster. ClG-*J*142040.3+395509 shows a strong signal in *Planck*.

7.9 ClG-*J*142138.3+382118

With a measured redshift of $z_{\mathrm{phot}} = 0.750 \pm 0.027$ ($z_{\mathrm{spec}} = 0.762$) and a richness of 41 ± 7, this cluster appears to be at higher redshift but with a comparable richness to RCS2-*J*232727.7−020437. Possible strong lensing arcs have been observed which also indicate a high mass. On the other hand, we cannot detect it at more than 3σ in the CARMA data, which could be due to the short integration time of only 1.3 h.

7.10 ClG-*J*152741.9+204443

ClG-*J*152741.9+204443 has a redshift of $z_{\mathrm{spec}} = 0.693$ and a richness of $N_{\mathrm{gal}} = 27 \pm 5$. This is a rather large richness, which also agrees with the CARMA analysis. There we find one of the strongest SZ signals, which corresponds to a mass of $M_{200} = (14.5 \pm 6.5) \times 10^{14} h_{70}^{-1}\,\mathrm{M}_{\odot}$. Again, this appears to be an exceptionally massive cluster.

8 CONCLUSIONS

We cross-correlated RASS and SDSS in order to find rich galaxy clusters at redshifts $0.6 \lesssim z \lesssim 1.0$. Using follow-up observations we confirmed 44 cluster candidates. The motivation was to find similar objects as RCS2-*J*232727.7−020437, in which we succeeded. We estimated red sequence redshifts which we compared to our spectroscopic sub-sample and determined the cluster richness by fitting and integrating a Schechter function.

In the end, we found at least two clusters of comparable richness as RCS2-*J*232727.7−020437. Furthermore, we achieved rough mass estimates from SZ observations for a sub-sample of 11 clusters and find them to be massive systems. Using the formalism by Mortonson et al. (2011) we find no tension between any of these clusters and the standard cosmological model. Further investigations, which will need deeper and higher quality observations, will reveal the masses of more of these rare objects and check whether those are compatible with the ΛCDM structure formation paradigm.

We have demonstrated that the approach of cross-correlating X-ray with optical data within an area of about 10 000 deg^2 is efficient resulting in the discovery of some of the richest galaxy clusters at high-z to date.

Our cluster sample is unique and complementary to the *Planck* cluster sample and also to the Southern hemisphere samples of the SPT and ACT. With respect to the redshift range and the large area this sample is more similar to the *Planck* sample than to the other two. Although we have constructed our sample by surveying a large area, we cannot attempt to infer cosmological parameters from it. The sample is by construction incomplete, because we searched for the most massive objects, which are easiest to detect.

ACKNOWLEDGEMENTS

AB was supported for this research partly through a stipend from the International Max Planck Research School (IMPRS) for Astronomy and Astrophysics at the Universities of Bonn and Cologne and through funding from the Transregional Collaborative Research Centre (TR 33) of the DFG.

CHG is supported by NSF grant AST-1140019.

TS acknowledges support from the German Federal Ministry of Economics and Technology (BMWi) provided through DLR under project 50 OR 1308.

HH is supported by the DFG Emmy Noether grant Hi 1495/2-1.

RGM is supported in part by the US Department of Energy under contract number DE-AC02-76SF00515.

THR acknowledges support from the DFG through the Heisenberg research grant RE 1462/5, from grant RE 1462/6, and from TR 33 (project B18).

The Dark Cosmology Centre is funded by the Danish National Research Foundation.

We would like to thank Douglas Applegate and Matthias Klein for fruitful discussions about the optical data and Chris Benn for his help with the ACAM data.

We thank Dominik Klaes and Inka Hammer for conducting early test observations for our project with the 1-m telescope of Bonn University at the Hoher List observatory as well as Patrick Kelly, who conducted test observations with the 2.1-m KPNO telescope. Also, we would like to thank Bas Nefs, who conducted test observations with the Isaac Newton Telescope.

We also thank Tom Plagge for his initial analysis of the CARMA data.

While preparing this paper, we made use of the PYTHON version of Ned Wright's cosmology calculator (Wright 2006), which was implemented by James Schombert. Additionally, we used TOPCAT (Taylor 2005) and STILTS (Taylor 2006).

For preparing this work, we made use of the following facilities and archives: the WHT, the LBT, the CARMA, the SDSS Archive, the *ROSAT* bright and faint source catalogues, the *Chandra* archive, and the *Planck* legacy archive.

Author contributions: AB led the optical reduction, redshift and richness analysis, cosmological comparison, and paper writing. TS conceived and led the overall programme and the optical follow-up campaign. RGM led the *Chandra* analysis. The CARMA observations, reductions, and analysis were conducted by CHG, MSo, and DM. JE created the y-maps from the *Planck* data. HHo, WH, AM, MSc, TE, HHi, AvdL contributed to the optical observations, reductions, and data analysis. THR and AH contributed to the further multiwavelength follow-up campaign. All authors have contributed to the writing of this paper.

REFERENCES

Ahn C. P. et al., 2014, ApJS, 211, 17
Aihara H. et al., 2011, ApJS, 193, 29
Andersson K. et al., 2011, ApJ, 738, 48
Angulo R. E., Springel V., White S. D. M., Jenkins A., Baugh C. M., Frenk C. S., 2012, MNRAS, 426, 2046
Arnaud M., Pratt G. W., Piffaretti R., Böhringer H., Croston J. H., Pointecouteau E., 2010, A&A, 517, A92
Bahcall N. A., Lubin L. M., Dorman V., 1995, ApJ, 447, L81
Bayliss M. B., Hennawi J. F., Gladders M. D., Koester B. P., Sharon K., Dahle H., Oguri M., 2011, ApJS, 193, 8

Benn C., Dee K., Agócs T., 2008, in McLean I. S., Casali M. M., eds, Proc. SPIE Conf. Ser. Vol. 7014, Ground-based and Airborne Instrumentation for Astronomy II. SPIE, Bellingham, p. 70146X
Bennett C. L. et al., 2003, ApJS, 148, 97
Benson B. A. et al., 2013, ApJ, 763, 147
Bertelli G., Bressan A., Chiosi C., Fagotto F., Nasi E., 1994, A&AS, 106, 275
Bertin E., Arnouts S., 1996, A&AS, 117, 393
Bleem L. E. et al., 2015, ApJS, 216, 27
Böhringer H. et al., 2007, A&A, 469, 363
Bonamente M., Joy M., LaRoque S. J., Carlstrom J. E., Nagai D., Marrone D. P., 2008, ApJ, 675, 106
Broadhurst T. J., Barkana R., 2008, MNRAS, 390, 1647
Brodwin M. et al., 2014, preprint (arXiv:e-prints)
Bruzual G., Charlot S., 2003, MNRAS, 344, 1000
Burenin R. A., Vikhlinin A., Hornstrup A., Ebeling H., Quintana H., Mescheryakov A., 2007, ApJS, 172, 561
Castander F. J., 1998, Ap&SS, 263, 91
Chabrier G., 2003, PASP, 115, 763
da Silva A. C., Kay S. T., Liddle A. R., Thomas P. A., 2004, MNRAS, 348, 1401
Duffy A. R., Schaye J., Kay S. T., Dalla Vecchia C., 2008, MNRAS, 390, L64
Ebeling H., Voges W., Bohringer H., Edge A. C., Huchra J. P., Briel U. G., 1996, MNRAS, 281, 799
Ebeling H., Edge A. C., Bohringer H., Allen S. W., Crawford C. S., Fabian A. C., Voges W., Huchra J. P., 1998, MNRAS, 301, 881
Ebeling H., Jones L. R., Fairley B. W., Perlman E., Scharf C., Horner D., 2001a, ApJ, 548, L23
Ebeling H., Edge A. C., Henry J. P., 2001b, ApJ, 553, 668
Ebeling H., Barrett E., Donovan D., Ma C.-J., Edge A. C., van Speybroeck L., 2007, ApJ, 661, L33
Ebeling H. et al., 2013, MNRAS, 432, 62
Erben T. et al., 2005, Astron. Nachr., 326, 432
Erben T. et al., 2009, A&A, 493, 1197
Erben T. et al., 2013, MNRAS, 433, 2545
Fitzpatrick M. J., 1993, in Hanisch R. J., Brissenden R. J. V., Barnes J., eds, ASP Conf. Ser. Vol. 52, Astronomical Data Analysis Software and Systems II. Astron. Soc. Pac., San Francisco, p. 472
Giallongo E. et al., 2008, A&A, 482, 349
Gilbank D. G., Gladders M. D., Yee H. K. C., Hsieh B. C., 2011, AJ, 141, 94
Gladders M. D., Yee H. K. C., 2000, AJ, 120, 2148
Gladders M. D., Yee H. K. C., 2005, ApJS, 157, 1
Gralla M. B. et al., 2011, ApJ, 737, 74
Haiman Z., Mohr J. J., Holder G. P., 2001, ApJ, 553, 545
Hasselfield M. et al., 2013, J. Cosmol. Astropart. Phys., 7, 8
High F. W. et al., 2010, ApJ, 723, 1736
Hildebrandt H. et al., 2010, A&A, 523, A31
Hildebrandt H. et al., 2012, MNRAS, 421, 2355
Hotchkiss S., 2011, J. Cosmol. Astropart. Phys., 7, 4
Jee M. J., Tyson J. A., 2009, ApJ, 691, 1337
Jee M. J. et al., 2011, ApJ, 737, 59
Kaiser N. et al., 2002, in Tyson J. A., Wolff S., eds, Proc. SPIE Conf. Ser. Vol. 4836, Survey and Other Telescope Technologies and Discoveries. SPIE, Bellingham, p. 154
Koester B. P. et al., 2007, ApJ, 660, 221
Mahdavi A., Hoekstra H., Babul A., Bildfell C., Jeltema T., Henry J. P., 2013, ApJ, 767, 116
Mantz A. B., Allen S. W., Morris R. G., Rapetti D. A., Applegate D. E., Kelly P. L., von der Linden A., Schmidt R. W., 2014, MNRAS, 440, 2077
Marrone D. P. et al., 2012, ApJ, 754, 119
Mehrtens N. et al., 2012, MNRAS, 423, 1024
Menanteau F. et al., 2013, ApJ, 765, 67
Milkeraitis M., van Waerbeke L., Heymans C., Hildebrandt H., Dietrich J. P., Erben T., 2010, MNRAS, 406, 673
Mortonson M. J., Hu W., Huterer D., 2011, Phys. Rev. D, 83, 023015
Motl P. M., Hallman E. J., Burns J. O., Norman M. L., 2005, ApJ, 623, L63
Muchovej S. et al., 2007, ApJ, 663, 708
Nagai D., Kravtsov A. V., Vikhlinin A., 2007, ApJ, 668, 1
Nastasi A. et al., 2014, A&A, 564, A17
Oguri M., Bayliss M. B., Dahle H., Sharon K., Gladders M. D., Natarajan P., Hennawi J. F., Koester B. P., 2012, MNRAS, 420, 3213
Paolillo M., Andreon S., Longo G., Puddu E., Gal R. R., Scaramella R., Djorgovski S. G., de Carvalho R., 2001, A&A, 367, 59
Pierre M. et al., 2001, The Messenger, 105, 32
Pierre M., Valtchanov I., Refregier A., 2002, in Jansen F. eds, New Visions of the X-ray Universe in the XMM-Newton and Chandra Era, ESA SP-488, preprint (arXiv:astro-ph/0202117)
Planck Collaboration XI, 2011, A&A, 536, A11
Planck Collaboration XII, 2011, A&A, 536, A12
Planck Collaboration III, 2013, A&A, 550, A129
Planck Collaboration XXIX, 2014, A&A, 571, A29
Planck Collaboration I, 2015, preprint (arXiv:e-prints)
Planck Collaboration XXVII, 2015, preprint (arXiv:e-prints)
Planck Collaboration XXIV, 2015, preprint (arXiv:e-prints)
Popesso P., Böhringer H., Brinkmann J., Voges W., York D. G., 2004, A&A, 423, 449
Postman M., Lubin L. M., Gunn J. E., Oke J. B., Hoessel J. G., Schneider D. P., Christensen J. A., 1996, AJ, 111, 615
Reiprich T. H., Böhringer H., 2002, ApJ, 567, 716
Remazeilles M., Delabrouille J., Cardoso J.-F., 2011, MNRAS, 410, 2481
Romer A. K., Viana P. T. P., Liddle A. R., Mann R. G., 2001, ApJ, 547, 594
Rudy D. J., Muhleman D. O., Berge G. L., Jakosky B. M., Christensen P. R., 1987, Icarus, 71, 159
Rykoff E. S. et al., 2014, ApJ, 785, 104
Schechter P., 1976, ApJ, 203, 297
Schirmer M., 2013, ApJS, 209, 21
Sehgal N. et al., 2013, ApJ, 767, 38
Sharon K. et al., 2015, preprint (arXiv:1503.07188)
Sievers J. L. et al., 2013, JCAP, 10, 60
Stanek R., Rasia E., Evrard A. E., Pearce F., Gazzola L., 2010, ApJ, 715, 1508
Sunyaev R. A., Zeldovich Y. B., 1970, Comments Astrophys. Space Phys., 2, 66
Sunyaev R. A., Zeldovich I. B., 1980, ARA&A, 18, 537
Taylor M. B., 2005, in Shopbell P., Britton M., Ebert R., eds, ASP Conf. Ser. Vol. 347, Astronomical Data Analysis Software and Systems XIV. Astron. Soc. Pac., San Francisco, p. 29
Taylor M. B., 2006, in Gabriel C., Arviset C., Ponz D., Enrique S., eds, ASP Conf. Ser. Vol. 351, Astronomical Data Analysis Software and Systems XV. Astron. Soc. Pac., San Francisco, p. 666
Tody D., 1993, in Hanisch R. J., Brissenden R. J. V., Barnes J., eds, ASP Conf. Ser. Vol. 52, Astronomical Data Analysis Software and Systems II. Astron. Soc. Pac., San Francisco, p. 173
Umetsu K. et al., 2014, ApJ, 795, 163
Vikhlinin A. et al., 2009, ApJ, 692, 1060
Voges W. et al., 1999, A&A, 349, 389
Voges W. et al., 2000, IAU Circ., 7432, 3
Waizmann J.-C., Redlich M., Bartelmann M., 2012, A&A, 547, A67
Waizmann J.-C., Ettori S., Bartelmann M., 2013, MNRAS, 432, 914
Weller J., Battye R. A., Kneissl R., 2002, Phys. Rev. Lett., 88, 231301
Wen Z. L., Han J. L., Liu F. S., 2012, ApJS, 199, 34
White S. D. M., Navarro J. F., Evrard A. E., Frenk C. S., 1993, Nature, 366, 429
Wright E. L., 2006, PASP, 118, 1711
Wright E. L. et al., 2010, AJ, 140, 1868

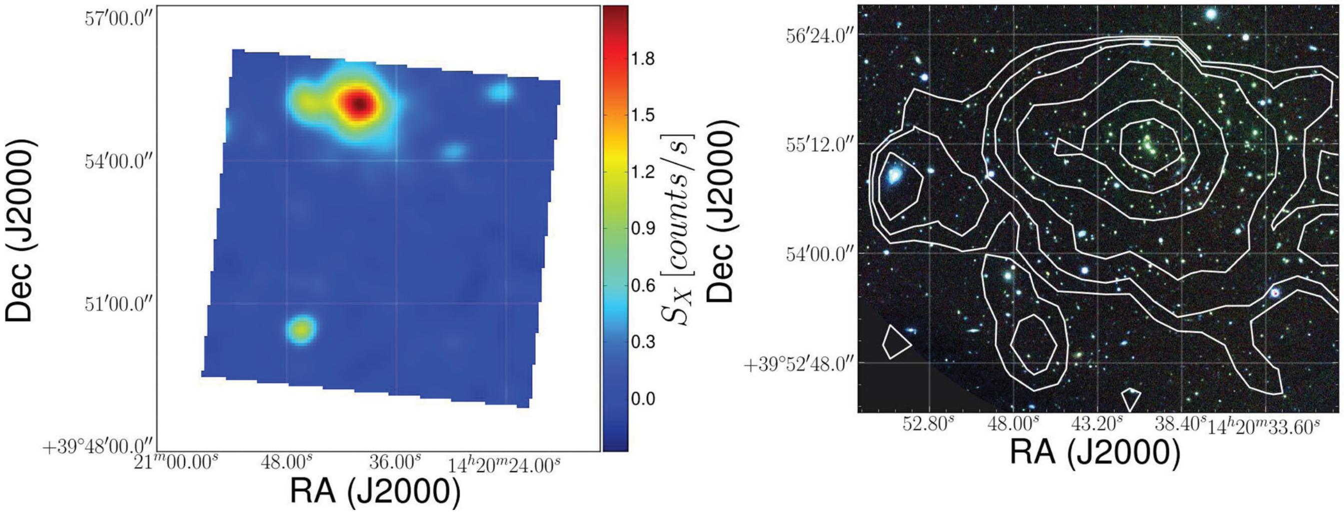

Figure A1. left: smoothed *Chandra* image of ClG-*J*142040.3+395509. Colour indicates the count rate. The cluster is visible in the upper part of the image. right: white lines are X-ray contours from *Chandra* superposed on the optical three-colour image from the WHT. This image shows a much smaller part of the field than visible in the left-hand panel, due to the small field of view in the optical. The contour levels are 0.05, 0.1, 0.2, 0.5, 1.0, and 1.5 counts s^{-1}.

APPENDIX A: X-RAY ANALYSIS OF CLG-*J*142040.3+395509

In addition to our optical and SZ data, we found serendipitous archival data from *Chandra* for ClG-*J*142040.3+395509. Fig. A1 shows the 0.6−7.0 keV count rate image. This was background subtracted and exposure corrected. When fitting a simple free absorption + thermal Bremsstrahlung model to the data we find the metallicity to be $0.5^{+0.4}_{-0.3}\,\mathrm{Z}_{\odot}$ and a temperature of $T_X = 8^{+3}_{-2}$ keV. This temperature as well as the high velocity dispersion from Bayliss et al. (2011) indicate a high mass. The flux in the 0.6–7.0 keV band is $S_X = 6.8 \times 10^{-13}\,\mathrm{erg\,cm^{-2}\,s}$. The 2–10 keV luminosity is $L_X = 8.1 \times 10^{44}\,\mathrm{erg\,s^{-1}}$ which is consistent with the RASS luminosity in Table B1. In Fig. A1, we also show the optical three-colour image superposed with the X-ray contours. Clearly, the X-ray peak coincides with the position of the BCG.

The chip, which is being analysed here is acis-S4, which is non-standard for the analysis of extended sources. This means that the calibration model is probably not as reliable as normal which might result in an additional systematic bias of our measurements. All errors given are 1σ errors.

APPENDIX B: GALAXY CLUSTER AND SZ DATA

Table B1. This table shows photometric and spectroscopic redshifts, richness, X-ray counts in 1 $\mathrm{s^{-1}}$ and the X-ray luminosity in $10^{44}\,\mathrm{erg\,s^{-1}}$ measured in the *ROSAT* 0.1-2.4keV band. N_{gal} is the richness measured using the Schechter function fit, N_{count} the one measured by counting galaxies brighter than $m^* + 2$. In the comments column, we have noted several anomalies, namely: ^{1} bimodal red sequence galaxy distribution as a function of redshift or only a weak signal (compare Fig. 3 top-right panel); ^{2} the data are shallow compared to other images; ^{3} the object had been observed at high airmass ($\approx$2); ^{4} the Schechter function fit did not work well, which means that our fixed parameters lead to poor fits. For clusters with known spectroscopic redshift, we used those instead of the photometric ones for the richness estimate. Values in brackets indicate the LBT values for clusters which have data from both telescopes. Coordinates given are those of the BCG. Cluster names showing the superscript † were independently discovered by Wen et al. (2012); the superscript $^\diamond$ indicates clusters that have been independently discovered by the *Planck* collaboration (Planck Collaboration XXVII 2015).

Object	WHT	LBT	SZ	Ra	Dec	z_{phot}	z_{spec}	N_{gal}	N_{count}	$\mathrm{counts_X}$	L_X	com.
ClG-J001640.6−130644†	x	–	–	00:16:40.636	−13:06:43.84	0.700 ± 0.097	–	18 ± 6	13 ± 4	0.0297 ± 0.0126	6.5 ± 3.1	1
ClG-J005805.6+003058	x	–	–	00:58:05.648	+00:30:57.85	0.725 ± 0.017	–	33 ± 6	39 ± 6	0.0230 ± 0.0099	5.5 ± 2.4	
ClG-J013710.4−103423	x	–	–	01:37:10.433	−10:34:23.15	0.525 ± 0.034	0.662	24 ± 5	17 ± 4	0.0192 ± 0.0091	2.9 ± 1.4	4
ClG-J031924.2+404055	x	–	–	03:19:24.237	+40:40:54.91	0.750 ± 0.020	0.680	6 ± 3	13 ± 4	0.0229 ± 0.0087	5.0 ± 1.9	1, 4
MACSJ074452.8+392725	x	–	–	07:44:52.775	+39:27:25.45	0.675 ± 0.028	0.698	19 ± 5	17 ± 4	0.0148 ± 0.0073	3.1 ± 1.5	
ClG-J080434.9+330509$^{\dagger\diamond}$	x	–	–	08:04:34.899	+33:05:08.99	0.575 ± 0.014	0.552	24 ± 5	26 ± 5	0.0239 ± 0.0102	3.0 ± 1.3	
ClG-J083415.3+452418†	–	x	x	08:34:15.317	+45:24:18.19	0.675 ± 0.029	0.666	19 ± 5	13 ± 4	0.0416 ± 0.0116	8.1 ± 2.3	
ClG-J084009.8+442154	x	–	–	08:40:09.783	+44:21:53.51	0.700 ± 0.060	–	21 ± 4	26 ± 5	0.0689 ± 0.0209	15.0 ± 5.0	2
ClG-J093503.2+061438	x	–	x	09:35:03.235	+06:14:38.46	0.750 ± 0.031	–	9 ± 3	8 ± 3	0.0435 ± 0.0135	11.2 ± 3.6	
ClG-J094742.3+351742	–	x	–	09:47:42.313	+35:17:41.81	0.500 ± 0.065	–	20 ± 4	2 ± 1	0.0190 ± 0.0086	1.8 ± 0.9	4
ClG-J094700.0+631905	x	–	–	09:47:00.010	+63:19:04.99	0.700 ± 0.062	0.710	9 ± 4	10 ± 3	0.0172 ± 0.0076	3.8 ± 1.8	4
ClG-J094811.6+290709	x	–	x	09:48:11.569	+29:07:09.48	0.775 ± 0.063	0.778	16 ± 4	21 ± 5	0.0337 ± 0.0109	9.5 ± 3.4	
ClG-J095416.5+173808	-	x	–	09:54:16.461	+17:38:07.76	0.725 ± 0.047	0.828	40 ± 6	15 ± 4	0.0216 ± 0.0110	6.5 ± 3.4	
ClG-J102714.5+034500	x	–	–	10:27:14.475	+03:45:00.36	0.700 ± 0.030	0.749	20 ± 5	33 ± 6	0.0304 ± 0.0126	7.4 ± 3.1	
ClG-J103605.6+441140	x	–	–	10:36:05.645	+44:11:40.29	0.800 ± 0.119	–	5 ± 3	13 ± 4	0.0228 ± 0.0100	6.9 ± 3.6	4
ClG-J104803.7+313843	–	x	x	10:48:03.669	+31:38:42.90	0.750 ± 0.047	–	31 ± 5	10 ± 3	0.0443 ± 0.0132	12.1 ± 3.9	
ClG-J120958.9+495352	x	x	x	12:09:58.948	+49:53:52.02	0.950(0.925) ± 0.112(0.027)	0.902	18(22) ± 5(5)	16(40) ± 4(6)	0.0486 ± 0.0145	20.3 ± 6.2	
ClG-J122208.6+422924	x	–	x	12:22:08.612	+42:29:24.19	1.000 ± 0.200	1.069	7 ± 4	12 ± 3	0.0189 ± 0.0087	11.3 ± 7.2	4
ClJ1226+33	x	–	–	12:26:58.170	+33:32:48.41	0.950 ± 0.028	0.892	14 ± 5	27 ± 5	0.0233 ± 0.0102	9.5 ± 4.2	
ClG-J124515.2+245335†	–	x	x	12:45:15.204	+24:53:35.41	0.650 ± 0.027	–	10 ± 4	15 ± 1	0.0233 ± 0.0100	4.2 ± 1.8	
ClG-J131104.8+551443	x	–	–	13:11:04.815	+55:14:42.67	0.775 ± 0.127	–	12 ± 5	10 ± 3	0.0204 ± 0.0080	5.7 ± 2.8	
ClG-J131339.7+221151	x	–	–	13:13:39.723	+22:11:50.82	0.675 ± 0.019	0.737	21 ± 5	25 ± 5	0.0232 ± 0.0106	5.3 ± 2.5	
ClG-J133620.3+544540	–	x	x	13:36:20.308	+54:45:40.22	0.875 ± 0.039	–	17 ± 4	20 ± 4	0.0204 ± 0.0088	7.7 ± 3.4	
ClG-J133732.5+195827	x	–	x	13:37:32.451	+19:58:26.57	0.900 ± 0.106	–	10 ± 5	11 ± 3	0.0162 ± 0.0079	6.5 ± 3.5	3
ClG-J135345.0+432905$^\diamond$	x	–	x	13:53:44.996	+43:29:05.12	0.725 ± 0.024	–	21 ± 6	42 ± 6	0.0393 ± 0.0107	9.3 ± 2.6	

Table B1 – *continued*

Object	WHT	LBT	SZ	Ra	Dec	z_{phot}	z_{spec}	N_{gal}	N_{count}	$\mathrm{counts}_{\mathrm{X}}$	L_X	com.
ClG-*J*142008.8−031906	x	–	–	14:20:08.763	−03:19:06.40	0.750 ± 0.070	–	16 ± 4	20 ± 4	0.0209 ± 0.0112	5.4 ± 3.0	
ClG-*J*142040.3+395509$^{\dagger\diamond}$	x	–	x	14:20:40.353	+39:55:09.72	0.600 ± 0.044	0.607	25 ± 5	34 ± 6	0.0360 ± 0.0100	5.5 ± 1.6	
ClG-*J*142138.3+382118$^{\diamond}$	x	–	x	14:21:38.288	+38:21:18.32	0.750 ± 0.027	0.762	41 ± 7	42 ± 6	0.0209 ± 0.0084	5.5 ± 2.3	2
ClG-*J*142227.4+233739	x	–	–	14:22:27.366	+23:37:38.82	0.750 ± 0.017	0.726	23 ± 5	20 ± 4	0.0284 ± 0.0105	6.9 ± 2.6	
ClG-*J*143411.9+175039	x	–	x	14:34:11.929	+17:50:38.96	0.800 ± 0.020	0.744	25 ± 7	35 ± 6	0.0278 ± 0.0101	7.4 ± 2.7	3
ClG-*J*144847.4+284312	x	–	–	14:48:47.381	+28:43:12.17	0.750 ± 0.125	–	3 ± 2	3 ± 2	0.0186 ± 0.0074	4.8 ± 2.4	1, 2, 3
ClG-*J*145508.4+320028	x	–	–	14:55:08.384	+32:00:27.90	0.675 ± 0.017	0.654	11 ± 4	27 ± 5	0.0161 ± 0.0068	3.0 ± 1.3	
ClG-*J*150532.2+331249†	x	–	–	15:05:32.212	+33:12:48.83	0.725 ± 0.036	0.757	24 ± 5	24 ± 5	0.0142 ± 0.0058	3.6 ± 1.5	
ClG-*J*151544.3+042554	x	–	–	15:15:44.312	+04:25:53.65	0.700 ± 0.039	–	32 ± 8	29 ± 5	0.0262 ± 0.0100	5.7 ± 2.2	
ClG-*J*151601.9+394426	x	–	x	15:16:01.946	+39:44:26.57	0.725 ± 0.025	–	10 ± 5	34 ± 6	0.0288 ± 0.0084	6.8 ± 2.0	2, 3, 4
ClG-*J*152741.9+204443	x	–	x	15:27:41.933	+20:44:42.77	0.700 ± 0.034	0.693	27 ± 5	14 ± 4	0.0269 ± 0.0122	5.8 ± 2.6	
ClG-*J*153035.0+130512	x	–	–	15:30:34.980	+13:05:12.31	0.625 ± 0.025	–	17 ± 4	34 ± 6	0.0216 ± 0.0103	3.6 ± 1.7	3, 4
ClG-*J*153258.8+021324	x	–	–	15:32:58.807	+02:13:23.87	0.850 ± 0.119	–	13 ± 3	12 ± 3	0.0209 ± 0.0086	7.3 ± 3.6	1, 3
ClG-*J*153735.6+382851	x	–	x	15:37:35.582	+38:28:50.90	0.750 ± 0.057	–	26 ± 5	29 ± 5	0.0336 ± 0.0116	8.7 ± 3.2	
ClG-*J*171225.8+561253	x	–	–	17:12:25.840	+56:12:52.51	0.600 ± 0.036	–	19 ± 5	13 ± 4	0.0082 ± 0.0036	1.2 ± 0.6	
ClG-*J*174109.9+555819	x	–	x	17:41:09.881	+55:58:19.06	0.625 ± 0.036	–	18 ± 5	27 ± 5	0.0059 ± 0.0023	1.0 ± 0.4	
ClG-*J*214826.3−053312	x	–	–	21:48:26.270	−05:33:12.01	0.625 ± 0.025	–	23 ± 5	34 ± 6	0.0211 ± 0.0095	3.5 ± 1.6	
ClG-*J*223007.6−080949	x	–	x	22:30:07.589	−08:09:48.80	0.575 ± 0.017	0.623	24 ± 5	25 ± 5	0.0336 ± 0.0154	5.1 ± 2.4	
ClG-*J*223727.5+135523	x	–	x	22:37:27.543	+13:55:22.56	0.700 ± 0.043	–	15 ± 5	24 ± 5	0.0161 ± 0.0067	3.5 ± 1.5	
ClG-*J*231215.6+035307	x	–	x	23:12:15.600	+03:53:06.90	0.625 ± 0.030	0.648	31 ± 6	19 ± 4	0.0234 ± 0.0093	4.1 ± 1.7	
ClG-*J*231520.6+090711	x	–	–	23:15:20.558	+09:07:11.09	0.725 ± 0.024	–	20 ± 5	36 ± 6	0.0206 ± 0.0086	4.9 ± 2.1	
RCS2-*J*232727.7−020437	x	x	–	23:27:27.7	−02:04:37.00	0.725(0.650) ± 0.042(0.024)	0.705	46(11) ± 7(6)	35(35) ± 6(6)	0.0474 ± 0.0137	10.7 ± 3.6	4(LBT)

Table B2. This table shows the results from the SZ observations. $t_{\rm int}$ is the integration time in hours. All masses are in $10^{14}h_{70}^{-1}\,{\rm M}_{\odot}$, $Y_{\rm SZ}$ is given in 10^{-5} Mpc^2. To the statistical mass errors from the fit, we have added in quadrature the 21 per cent scatter from the scaling relation from Andersson et al. (2011). We acknowledge the fact that our error bars do not include the 20 per cent systematic error from the uncertainty in the high-redshift mass calibration (see Section 5).

Object	$z_{\rm spec}$	$z_{\rm phot}$	$Y_{\rm SZ}$	M_{500}	M_{200}	$t_{\rm int}$
ClG-*J*083415.3+452418	0.666	0.675	2.9 ± 1.1	3.8 ± 1.2	5.6 ± 2.0	3.5
ClG-*J*094811.6+290709	0.778	0.775	8.2 ± 1.7	6.6 ± 1.9	10.4 ± 3.3	4.1
ClG-*J*095416.5+173808	0.828	0.725	<5.4	<5.1	<8.0	4.0
ClG-*J*104803.7+313843	–	0.750	16.8 ± 3.6	9.8 ± 3.2	16.0 ± 5.5	3.5
ClG-*J*120958.9+495352	0.902	0.950	5.9 ± 1.2	5.3 ± 1.5	8.3 ± 2.5	6.8
ClG-*J*122208.6+422924	1.069	1.000	<3.7	<3.8	<5.8	4.0
ClG-*J*124515.2+245335	–	0.650	5.3 ± 1.7	5.3 ± 1.6	8.1 ± 2.8	4.1
ClG-*J*131339.7+221151	0.737	0.675	2.1 ± 0.9	3.1 ± 1.0	4.4 ± 1.8	5.8
ClG-*J*133620.3+544540	–	0.875	<1.9	<2.8	<4.0	3.6
ClG-*J*133732.5+195827	–	0.900	8.2 ± 1.2	6.4 ± 1.8	10.2 ± 3.0	1.4
ClG-*J*135345.0+432905	–	0.725	12.3 ± 6.8	8.3 ± 3.5	13.4 ± 6.0	1.6
ClG-*J*142040.3+395509	0.607	0.600	<7.0	<6.2	<9.7	1.5
ClG-*J*142138.3+382118	0.762	0.750	<9.7	<7.2	<11.5	1.3
ClG-*J*143411.9+175039	0.744	0.800	<7.5	<6.3	<9.9	1.7
ClG-*J*151601.9+394426	–	0.725	<7.5	<6.3	<9.9	0.9
ClG-*J*152741.9+204443	0.693	0.700	14.0 ± 7.6	9.0 ± 3.8	14.5 ± 6.5	1.8
ClG-*J*153735.6+382851	–	0.750	3.6 ± 0.8	4.2 ± 1.1	6.3 ± 1.9	5.1
ClG-*J*174109.9+555819	–	0.625	<10.5	<7.8	<12.4	4.5
ClG-*J*223007.6−080949	0.623	0.575	<4.4	<4.8	<7.3	3.4
ClG-*J*223727.5+135523	–	0.700	<2.5	<3.4	<5.0	6.3
ClG-*J*231215.6+035307	0.648	0.625	1.9 ± 0.9	3.0 ± 1.0	4.2 ± 1.8	6.8

APPENDIX C: POSTAGE STAMPS OF ALL CLUSTERS

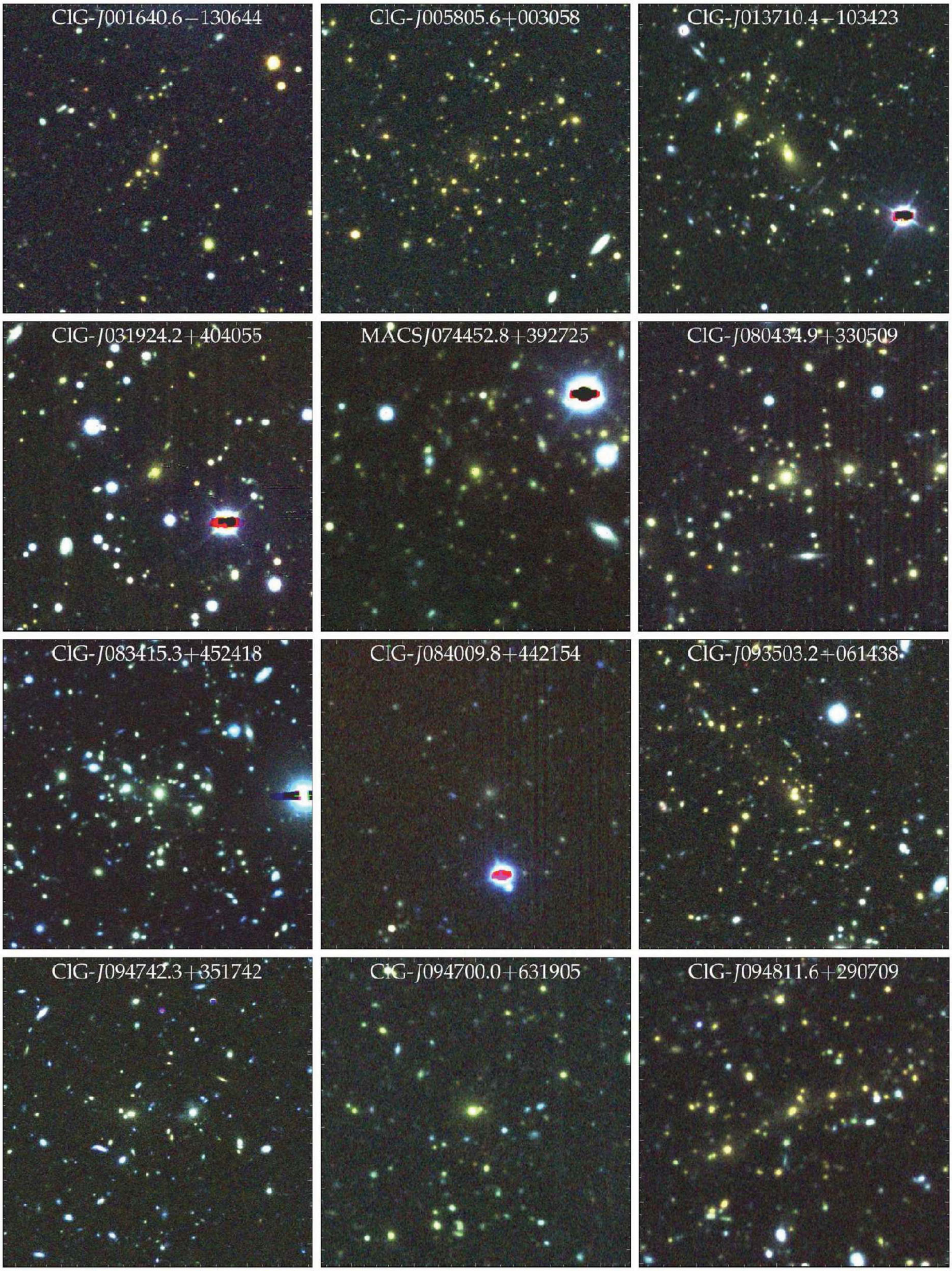

Figure C1. In this figure, we present optical postage stamps of all clusters in our sample. These postage stamps were created using the *r*-, *i*-, and *z*-band images from WHT and LBT. Wherever available we show the LBT data, which is considerably deeper. Which data are available can be found in Table B1. All images show the inner 1.7 arcmin of the cluster.

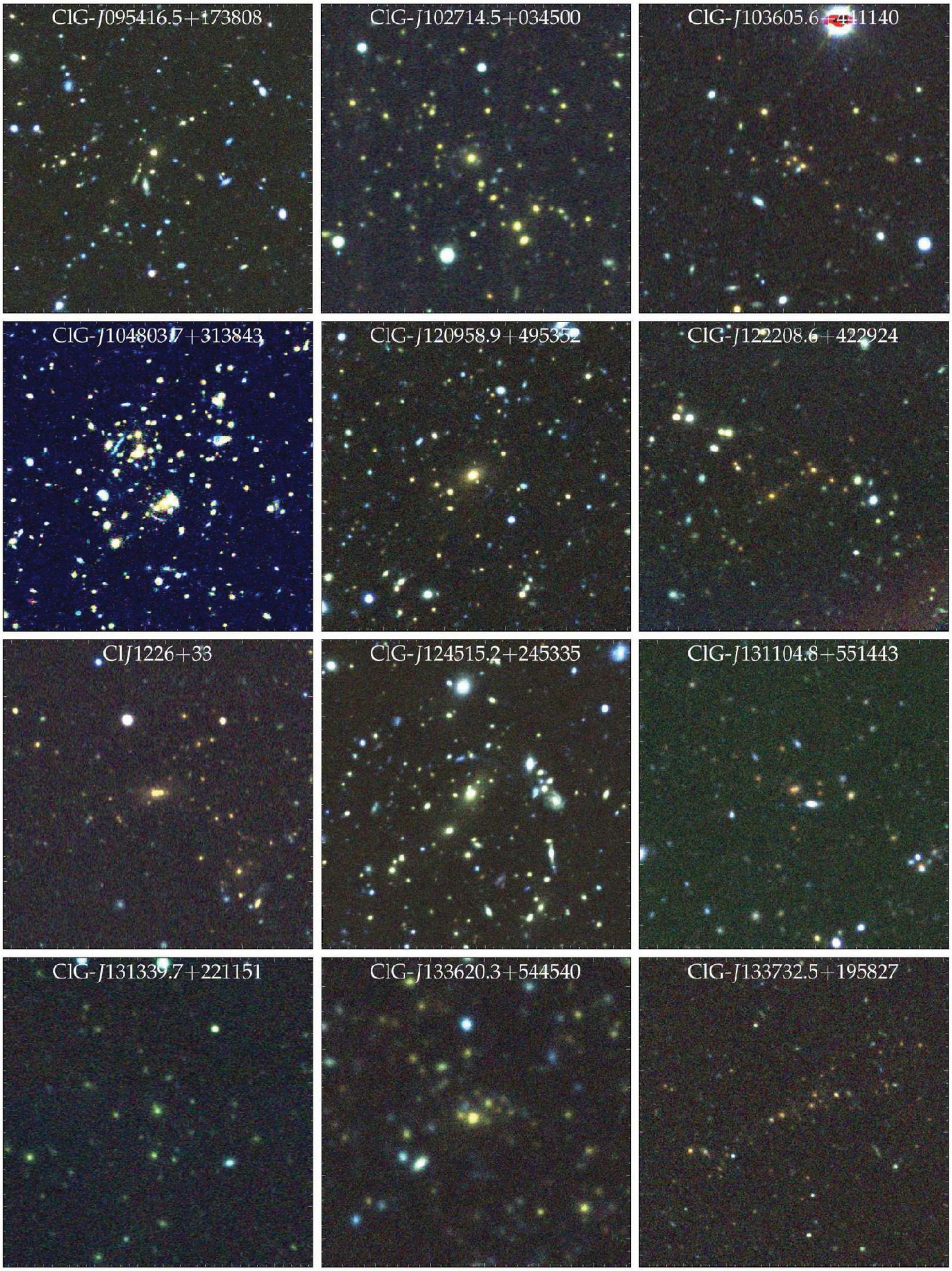

Figure C1 – *continued*

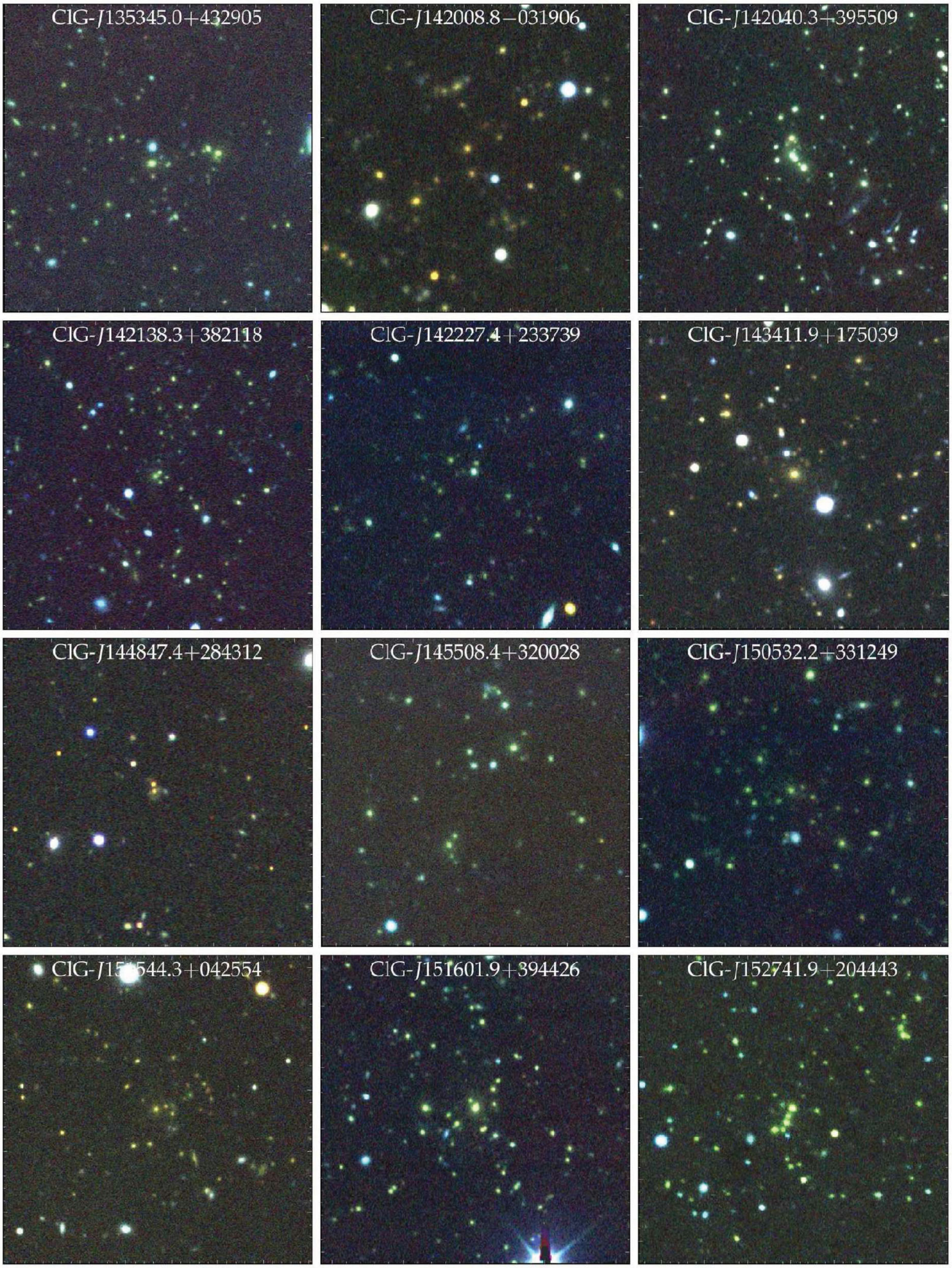

Figure C1 – *continued*

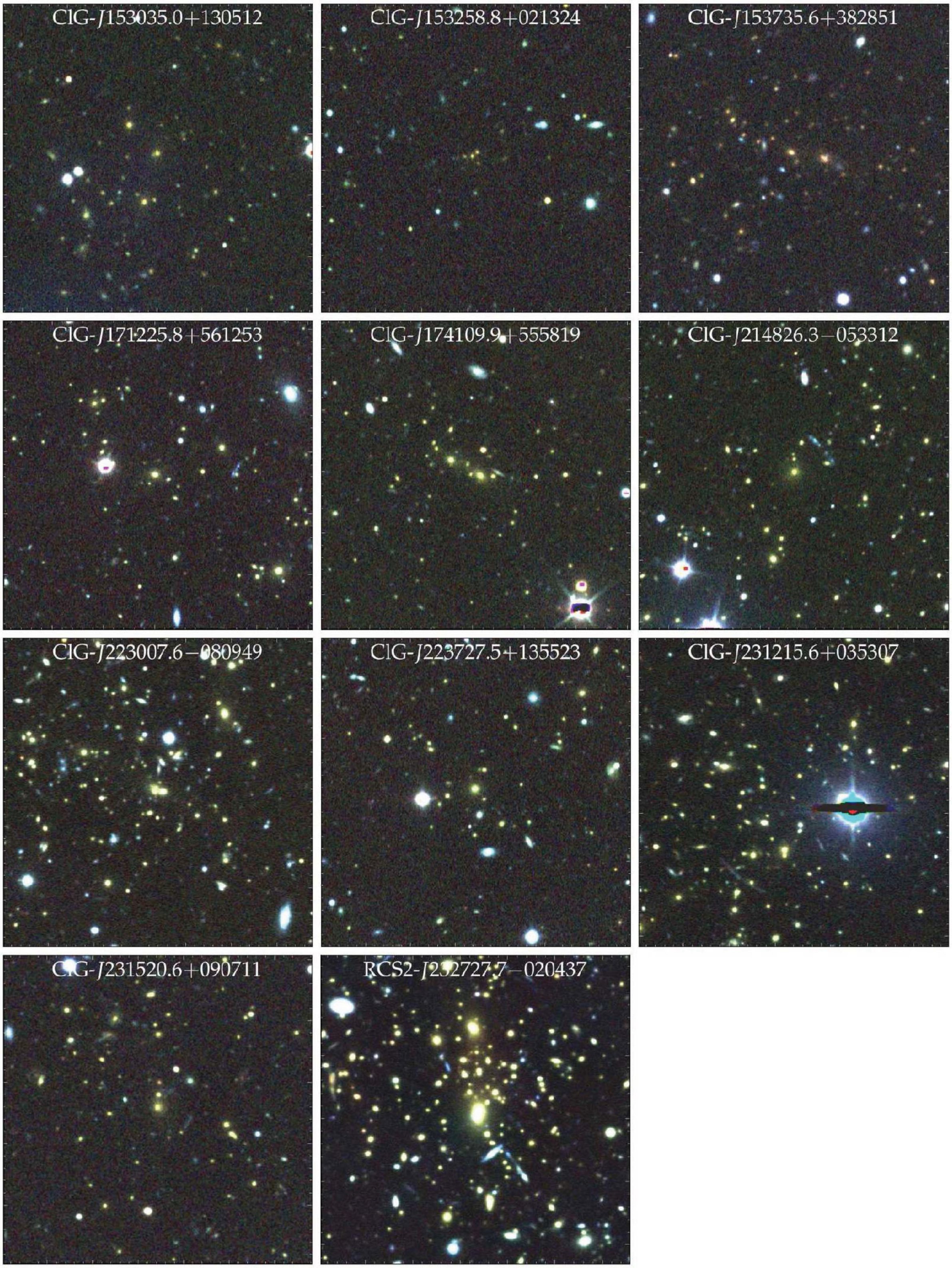

Figure C1 – *continued*

APPENDIX D: MAPS FROM THE CARMA DATA

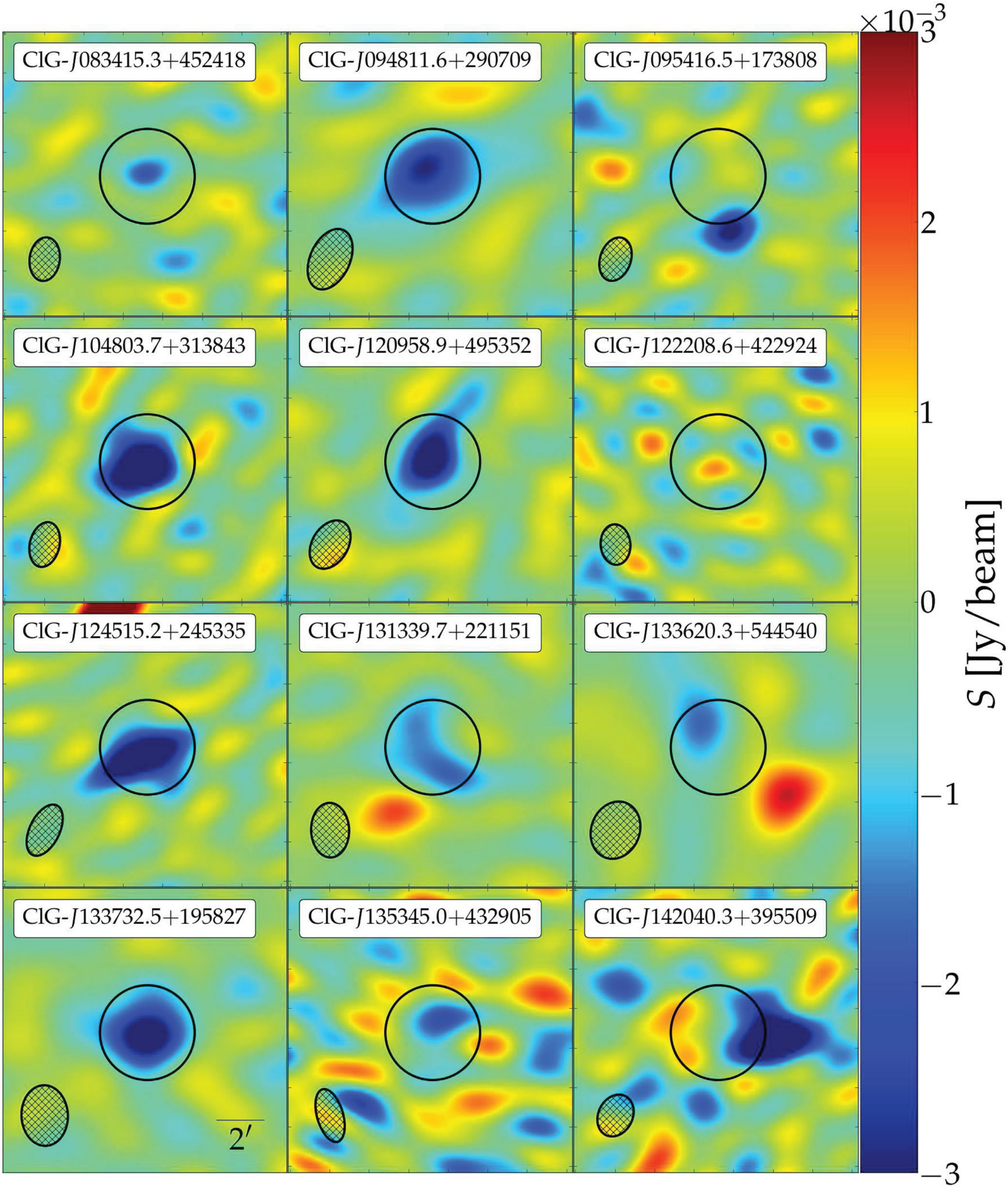

Figure D1. We show SZ-maps for all clusters observed with CARMA. The images show 12 × 12 arcmin^2. The ellipses in the bottom left are the beams, the circle in the centre has a 2 arcmin radius and indicates the BCG position.

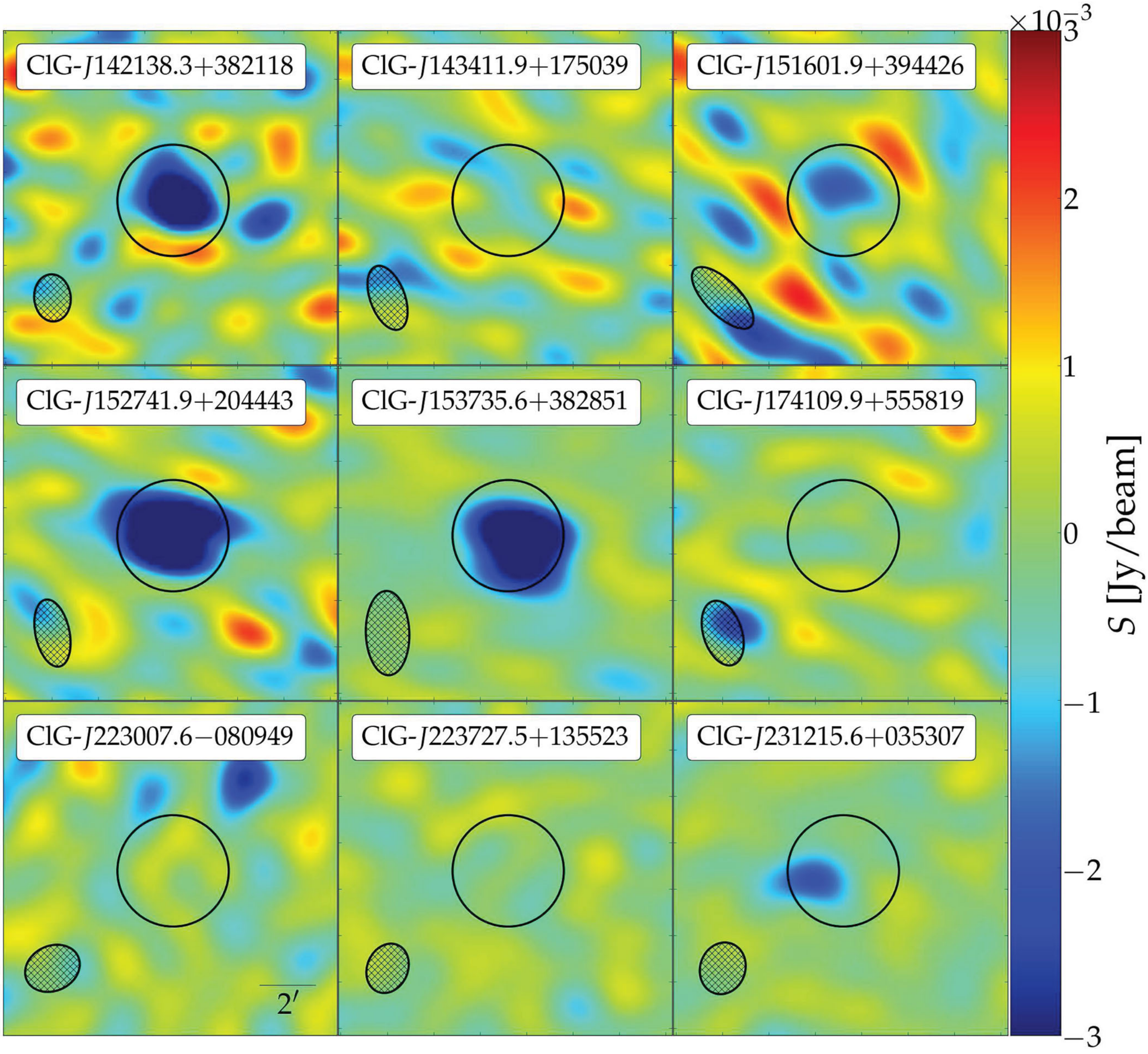

Figure D1 – *continued*

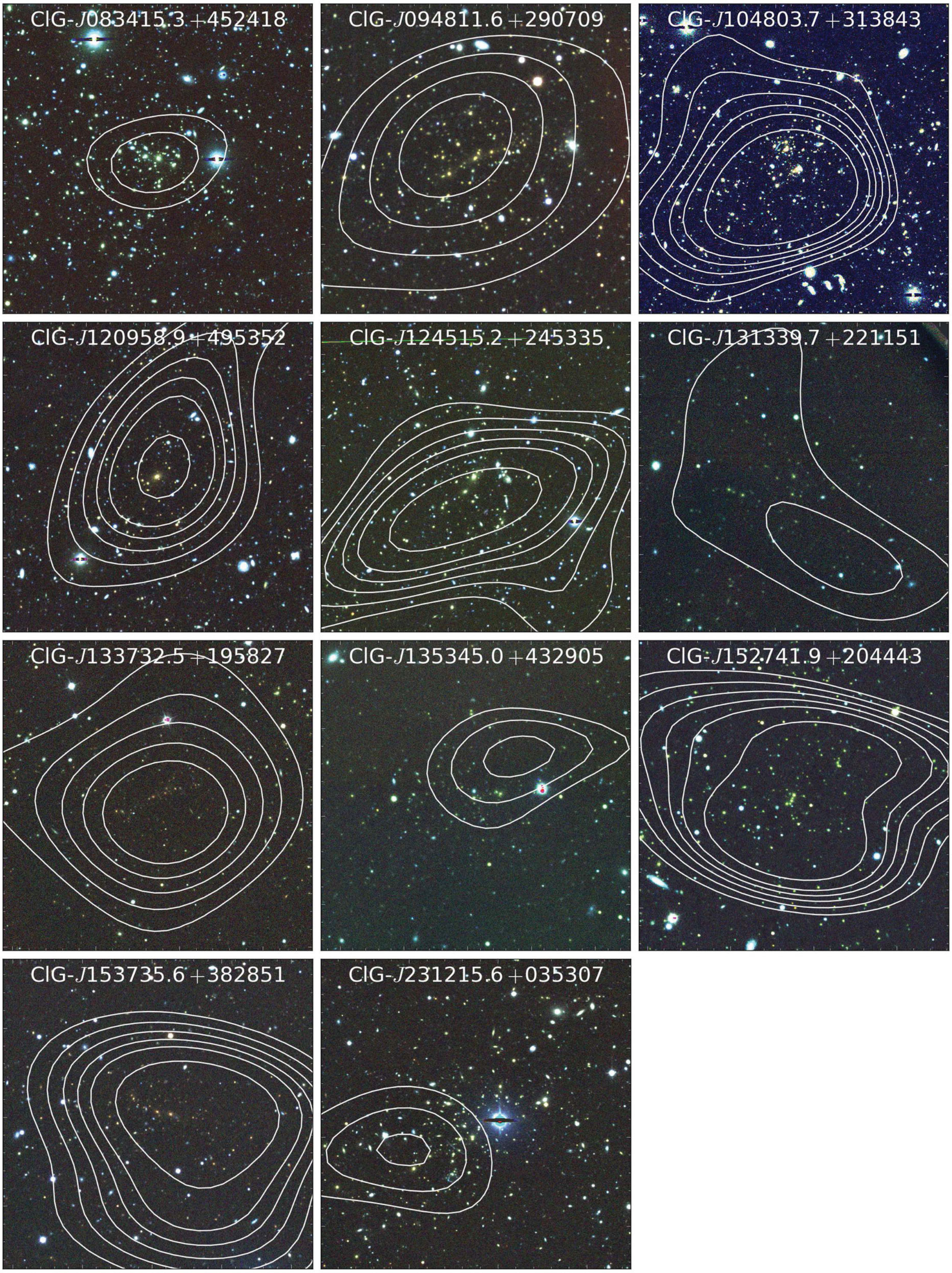

Figure D2. We show optical three-colour images and the corresponding SZ-overlay for all clusters that have been detected at more than 3σ with CARMA. The images show 4.2 arcmin × 4.2 arcmin around the BCG. The contour levels are -4.0, -3.0, -2.5, -2.0, -1.5, and -1.0×10^{-3} Jy beam^{-1}.

APPENDIX E: RESULTS FROM *PLANCK* DATA

We constructed 10° × 10° y-maps of all 44 galaxy clusters from public *Planck* data by forming a linear combination of maps (the ILC method; Bennett et al. 2003; Remazeilles, Delabrouille & Cardoso 2011), using all six frequency bands of the *Planck* High Frequency Instrument, taken from the recent 2015 data release (Planck Collaboration I 2015).

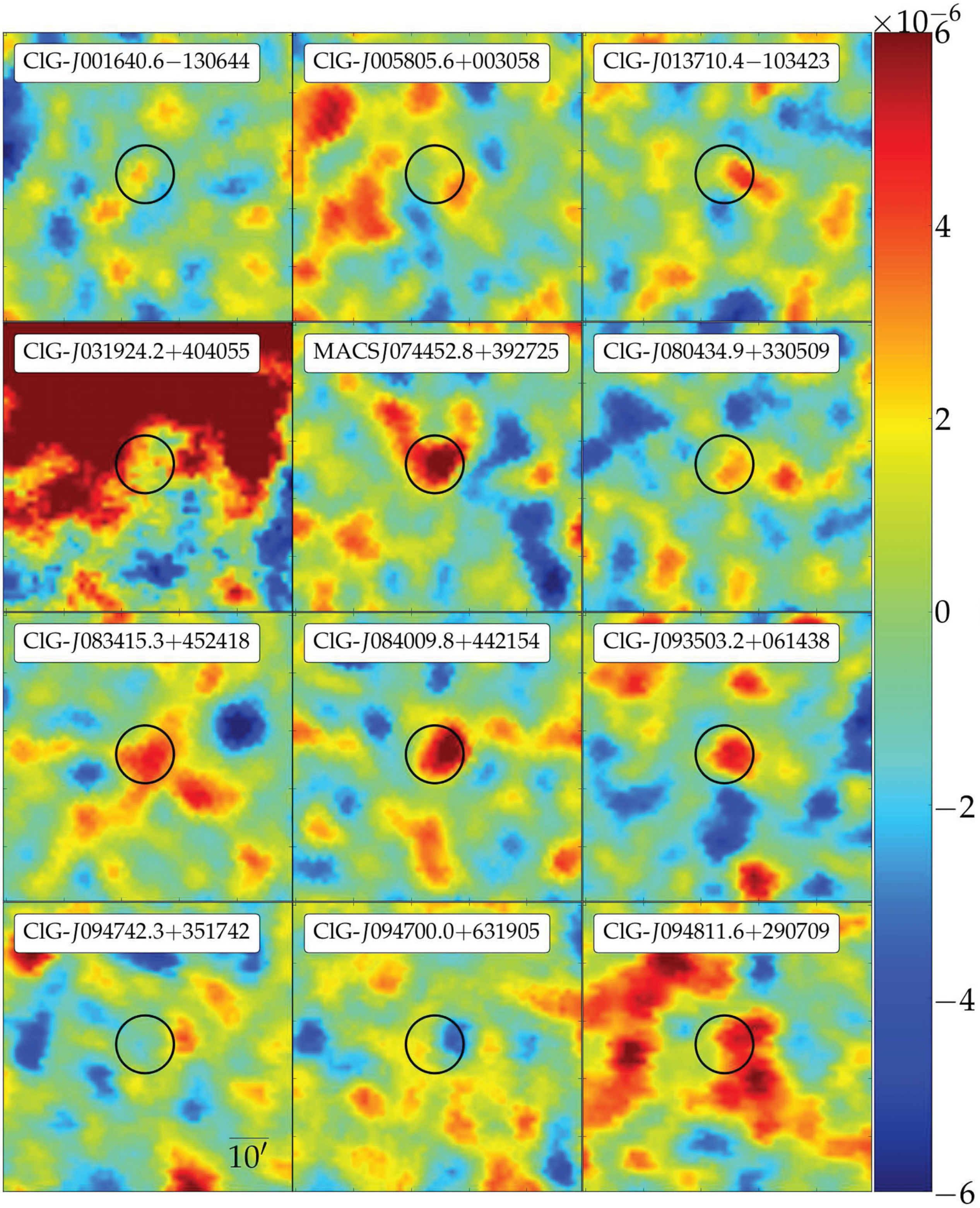

Figure E1. This figure shows the y-maps of all the clusters in our sample in *Planck*. The images show a 1.25 × 1.25 deg^2 field around the cluster. The black circle has a 7.5 arcmin radius and is centred at the BCG.

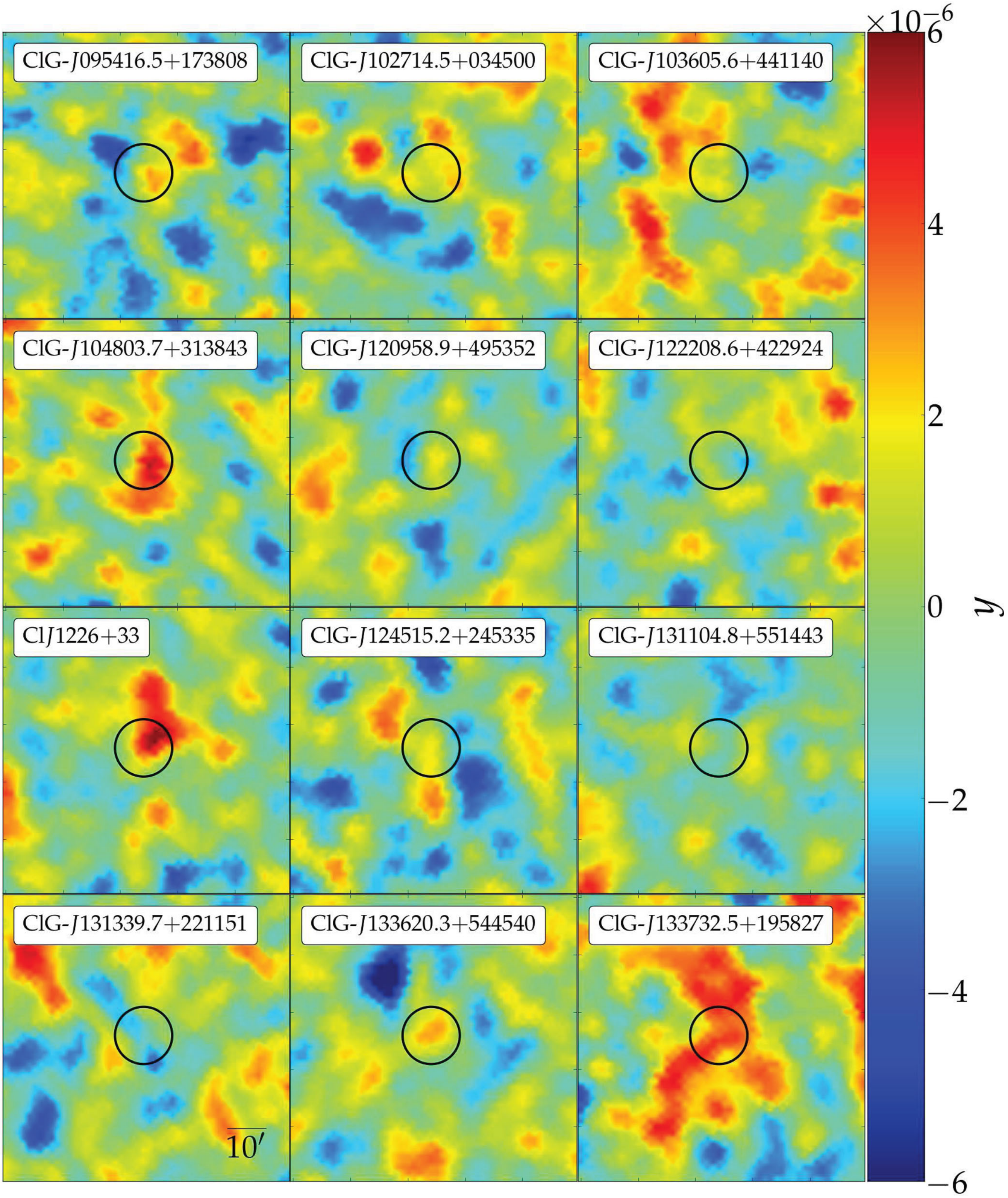

Figure E1 – *continued*

A Gaussian filter was applied to smooth all maps to a common resolution of 10 arcmin, corresponding to the *Planck* beam at 100 GHz. The final Compton-y maps are the weighted sum of all six maps: $y = \sum_i \omega_i T_i / T_{\mathrm{CMB}}$. Here T_i are the individual channel maps, each weighted with an ILC-coefficient ω_i. The coefficients are chosen to minimize the variance of the reconstructed Compton-y map while fulfilling two constrains: (1) eliminate the primary CMB Temperature anisotropies and (2) preserve the temperature

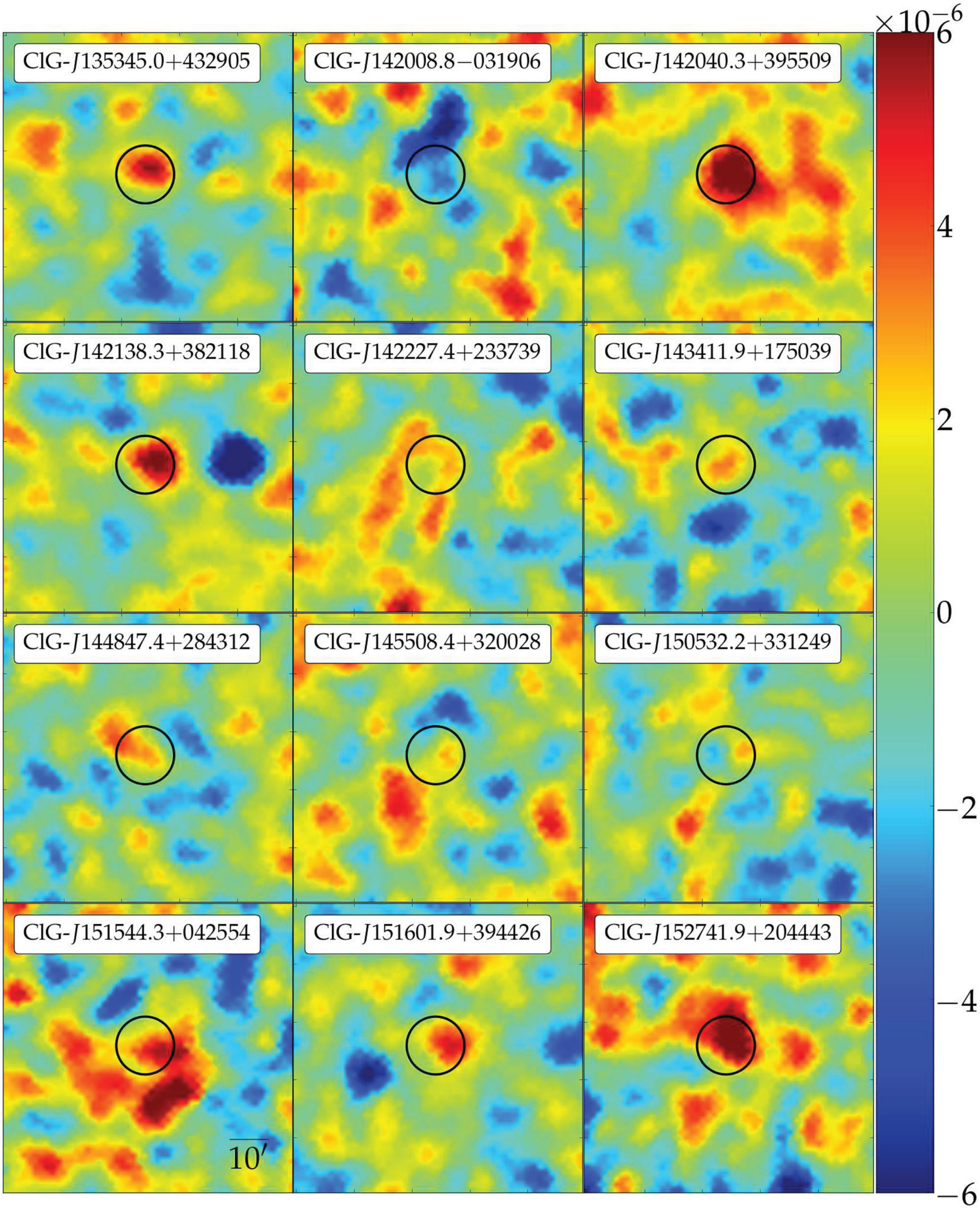

Figure E1 – *continued*

fluctuations introduced by the SZE. The produced map may contain an offset, since the variance of the map stays unaffected while adding a constant. The map offset was determined by fitting the histogram of pixel values with a Gaussian, which provides a very good model for the map noise. The offset is then corrected for by subtracting the mean of the Gaussian. In Fig. E1, we show *Planck* y-maps for all clusters, which have been observed with CARMA.

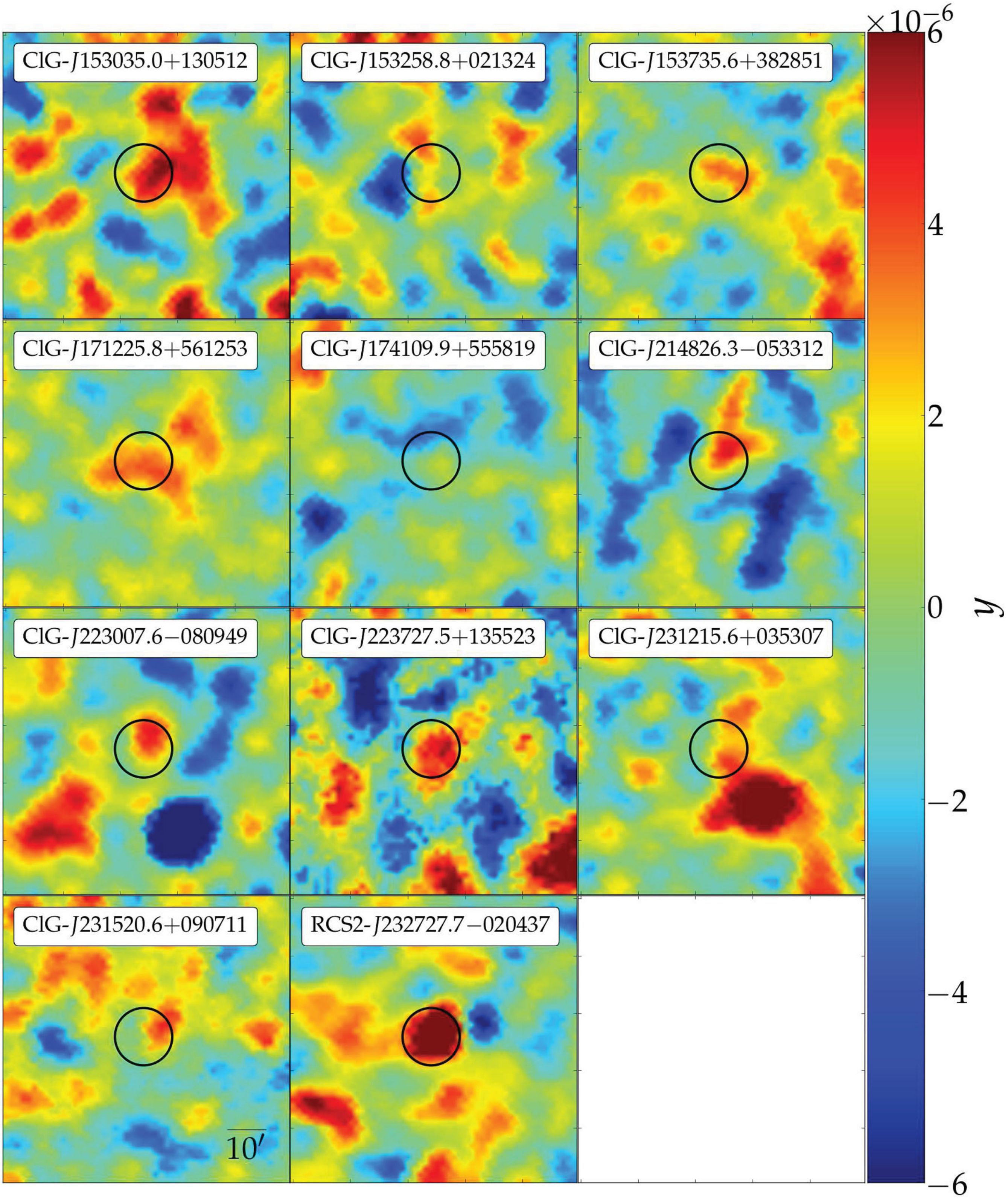

Figure E1 – *continued*

This paper has been typeset from a TEX/LATEX file prepared by the author.